Article

Not peer-reviewed version

Use of SWOT Data for Hydrodynamic Modelling in a Tropical Microtidal Estuarine System: The Case of Casamance (Senegal)

Amadou DIOUF *, Edward Salameh *, Issa Sakho, Bamol Ali Sow, Julien Deloffre, Carlos López Solano, Imen Ema Turcki, Robert Lafite *

Posted Date: 30 July 2025

doi: 10.20944/preprints202507.2525.v1

Keywords: Casamance estuary; Hydrodynamic modelling; SWOT satellite; Multi-source validation

 doi:10.20944/preprints202507.2525.v1

Article

Use of SWOT Data for Hydrodynamic Modelling in a Tropical Microtidal Estuarine System: The Case of Casamance (Senegal)

Amadou Diouf [1], Edward Salameh [2,*], Issa Sakho [3], Bamol Ali Sow [2], Julien Deloffre [2], Carlos López Solano [2], Imen Ema Turcki [2] and Robert Lafite [2]

[1] Laboratoire d'Océanographie, des Sciences de L'Environnement et du Climat (LOSEC), Université Assane Seck de Ziguinchor, BP 523, Ziguinchor, Sénégal

[2] UNIROUEN, CNRS, UMR 6143–M2C, Université de Normandie, 76000 Rouen, France

[3] Laboratory of Scientific Computing, Modelling, Environment and Sustainable Development, Training and Research Unit Science and Advanced Technologies, Amadou Mahtar Mbow University, Diamniadio, Senegal, Street 21x20, 2nd District, Urban Pole of Diamniadio - BP: 45927 Dakar NAFA VDN, Dakar, Senegal

* Correspondence: edward.salameh@cnrs.fr

Abstract

Since the early 1990s, satellite altimetry has significantly improved our understanding of coastal and estuarine dynamics. The Casamance estuary in Senegal exemplifies a tropical microtidal system with limited instrumentation despite pressing environmental, social, and navigational concerns. This study explores the potential of SWOT satellite data to support the calibration and validation of high-resolution hydrodynamic models. Multi-source dataset of in-situ measurements and altimetry observations has been combined with numerical modelling to investigate the hydrodynamics in reponse to physical drivers. Statistical metrics were used to quantify model performance. Results show that SWOT accurately captures water level variations in the main channel (width 800 m to 5 km), including both tidal and non-tidal contributions, with high correlation (R = 0.90) and low error (RMSE < 0.25 m). Performance decreases in tributaries (R = 0.42, RMSE up to 0.34 m), due to interpolated bathymetry and complex local dynamics. Notably, Delft3D achieves R = 0.877 at Diogué (RMSE = 0.204 m) and R = 0.843 at Carabane (RMSE = 0.225 m). These findings highlight the strategic value of SWOT for improving hydrodynamic modelling in data-scarce estuarine environments.

Keywords: casamance estuary; hydrodynamic modelling; SWOT satellite; multi-source validation

1. Introduction

The Casamance estuary, located in the tropics, is characterised by a microtidal regime and inverse salinity dynamics [1–4]. Its hydrodynamics are governed by complex flows arising from the interactions between tidal forcing and seasonal hydrological variations [5,6]. A thorough understanding of these processes is essential for wetland management, flood risk mitigation, and assessing climate change impacts. However, modelling water levels in such tropical estuaries remains challenging due to the scarcity of in situ data and limitations of traditional hydrodynamic models.

Satellite altimetry has become a critical tool for the spatio-temporal monitoring of water level variations in continental hydrological systems, facilitating improved understanding and management of water resources. Joint analyses of ICESat and ICESat-2 data have revealed significant water level increases in numerous lakes and rivers worldwide. For example, [7] documented a 3.66 m rise in Qinghai Lake's level between 2004 and 2020, equating to an average increase of 0.23 m yr^{-1}.

Similarly, [8] estimated that among over 22,000 water bodies exceeding 1 km^2, approximately 78% of natural lakes and 56% of artificial reservoirs exhibited upward water level trends between 2003 and 2021, with a global average increase of +0.02 ± 0.02 m yr^{-1} . Seasonal fluctuations were more

 doi:10.20944/preprints202507.2525.v1

pronounced in reservoirs, indicating substantial anthropogenic influence. Moreover, [9] demonstrated robust relationships between water levels and surface area variations through combined GLAS and MODIS data, exemplified by the Danjiangkou reservoir. In another study, [10] documented an ~8 m increase in Lake Ngangzi (Tibet) between 1998 and 2017, with varying rates over different periods.

In Africa, where in situ hydrological networks remain limited, satellite altimetry and optical imagery are indispensable for monitoring water resources [11,12], coastal topography evolution [13–25], water level variation [23,26–28], and biodiversity monitoring [29].

Since the 1990s, radar altimetry has been an essential method for large-scale hydrological monitoring. Originally designed for sea surface height measurement, it has progressively adapted to inland water monitoring, including lakes, rivers, and floodplains [30–32]. Radar altimetry estimates water surface elevation by measuring the round-trip travel time of radar pulses reflected from water surfaces, achieving centimetre-level accuracy over wide, open areas. Unlike laser altimetry, radar altimetry is largely unaffected by light and weather conditions, making it particularly suitable for tropical regions characterised by persistent cloud cover [32]. This capability has been pivotal in addressing data gaps in hydrological characterisation across West Africa. In tropical basins, radar altimetry has proven valuable for detecting seasonal water level variations, deriving river discharge via height-discharge relationships, and identifying flood and drought events [31,33].

Missions such as TOPEX/Poseidon, ENVISAT, Jason-2/3, SARAL/AltiKa, and Sentinel-3 have been successfully used to analyse hydrological dynamics in major basins including the Amazon, Niger, and Ogooué [32,34]. However, estuarine environments pose additional challenges for radar altimetry due to proximity to coastlines, altering dry/wet zones, tidal contamination of signals, and complex channel geometries. Recent advances in waveform retracking have improved water level retrieval accuracy in such complex environments, as demonstrated in the Ganges-Brahmaputra estuary [35]. These improvements take into account the aliasing effects and enable observation of tidal-fluvial interactions with resolution sufficient for hydrodynamic model validation and calibration.

The Surface Water and Ocean Topography (SWOT) mission, launched in December 2022, represents a significant leap forward in satellite observation of inland and coastal waters. Employing Ka-band radar interferometry (KaRIn), SWOT provides two-dimensional water surface elevation maps with spatial resolutions of 50–100 m and an 11-day revisit cycle [35–43]. This unprecedented capability facilitates monitoring of hydrological dynamics in estuaries, floodplains, and small tropical rivers, previously inaccessible to conventional altimeters.

Early studies have demonstrated SWOT's potential to estimate water levels and assimilate data into flood and sediment transport models [44], as well as to characterise fine-scale oceanic eddies [45,46]. These advances are particularly relevant for the Casamance estuary, where scarce in situ data and pronounced seasonal hydro-sedimentary processes shape morphodynamics.

In the Casamance estuary (Senegal), tidal processes strongly influence hydrodynamics [47–50]. SWOT satellite data offer valuable insights into water level variability by complementing tide gauge observations, enhancing understanding of complex oceanic and fluvial interactions. Integrating SWOT data into hydrodynamic models enables improved calibration and validation, reducing uncertainties associated with hydrological and morphological parameters, and thereby enhancing forecast reliability.

This article evaluates the contribution of SWOT altimetry to water level quantification in the Casamance estuary by using SWOT-derived water surface elevations to validate and compare the performance of two models: (i) a high-resolution Delft3D numerical model and (ii) the global TPXO8 tidal model.

Delft3D solves the Navier–Stokes equations and is widely used for coastal and estuarine modelling, while TPXO8 is a global tidal solution derived from satellite altimetry and optimised for tidal simulations. The analysis focuses on identifying areas of agreement and divergence along the estuarine gradient.

 doi:10.20944/preprints202507.2525.v1

Additionally, the study includes a morphological validation of the Delft3D model through the quantification of sediment transport and distribution under tidal influence. By assessing simulated sediment fluxes and deposition patterns against observational data, this approach enables a better understanding of morphodynamic processes shaping the estuary. Incorporating both hydrodynamic and morphodynamic validations strengthens the overall model reliability for predicting estuarine evolution under natural forcings.

2. Materials and Methods

2.1. Study Area

The Casamance estuary, situated in southern Senegal between latitudes 12°20′N and 12°50′N, is a tropical estuarine system characterised by a microtidal regime. It experiences minimal anthropogenic influence and minimal exposure to the oceanic swell, which is significantly dissipated at the entrance to the Casamance. The estuary extends for approximately 200 km from its Atlantic mouth to the upstream areas near Kolda. Upstream, the river is approximately 4 km wide and narrows near Ziguinchor (640 m) before widening again towards the mouth, where it can reach 8 km [51].

The system exhibits a complex morphology, characterised by a main channel of sinuous configuration, accompanied by numerous lateral branches (up to 500 m wide) that serve as conduits for rivers and irrigated rice fields (Figure 1). In addition, the system features bolongs, which are more than 50 m wide and extend for several kilometers, further contributing to the complexity of the hydrological network. A bolong is defined as a natural or secondary tidal channel carrying salt or brackish water. These channels are characteristic of the low-lying coastal areas of Casamance (Senegal) and The Gambia. Connected to the main estuary and often fringed by mangroves, a bolong plays a key role in the circulation of water, sediments, and nutrients. It ensures a dynamic hydrological link between the estuary, freshwater tributaries, and rice fields or wetland areas, contributing to salinity regulation, the flooding and drainage of agricultural zones, and the overall functioning of coastal ecosystems. Extensive areas of mangroves are present in this region, playing a crucial role in hydrosedimentary regulation and the preservation of local biodiversity. The estuary is home to fisheries areas and marine protected areas (Kassa-Blantaounda and Niamone-Kalounaye), although it is locally subject to anthropogenic contamination [52].

The hydrological regime is characterised by significant seasonal variability, with high river flows during the rainy season (June to October) and very low or even zero flows in the dry season (November to May) [5,6,53,54]. During the previous hydrological half-cycle (1970-2013), the maximum annual flow recorded at the Kolda hydrometric station was 45 m^3/s [49].

Sedimentological analysis of the Casamance estuary reveals a longitudinal distribution into three major provinces [55,56].The downstream areas are characterised by well-sorted sands with low lutitics, while the intermediate areas exhibit heterogeneous sediments, comprising coarse sands, shell fragments and gravels. In the upstream region, the deposits are predominantly composed of sand and gravel, with the gravel accumulating at the base of the channels.

The semi-diurnal tide exhibits a moderate amplitude at the mouth (approximately 1.5 m) that gradually diminishes upstream. This phenomenon is accompanied by tidal wave distortion phenomena [49,50], due to the combined effects of channel geometry, bottom friction and low river inputs. The Casamance estuary is an ideal natural laboratory for the study of hydrodynamic dynamics in tropical systems with low tidal ranges.

 doi:10.20944/preprints202507.2525.v1

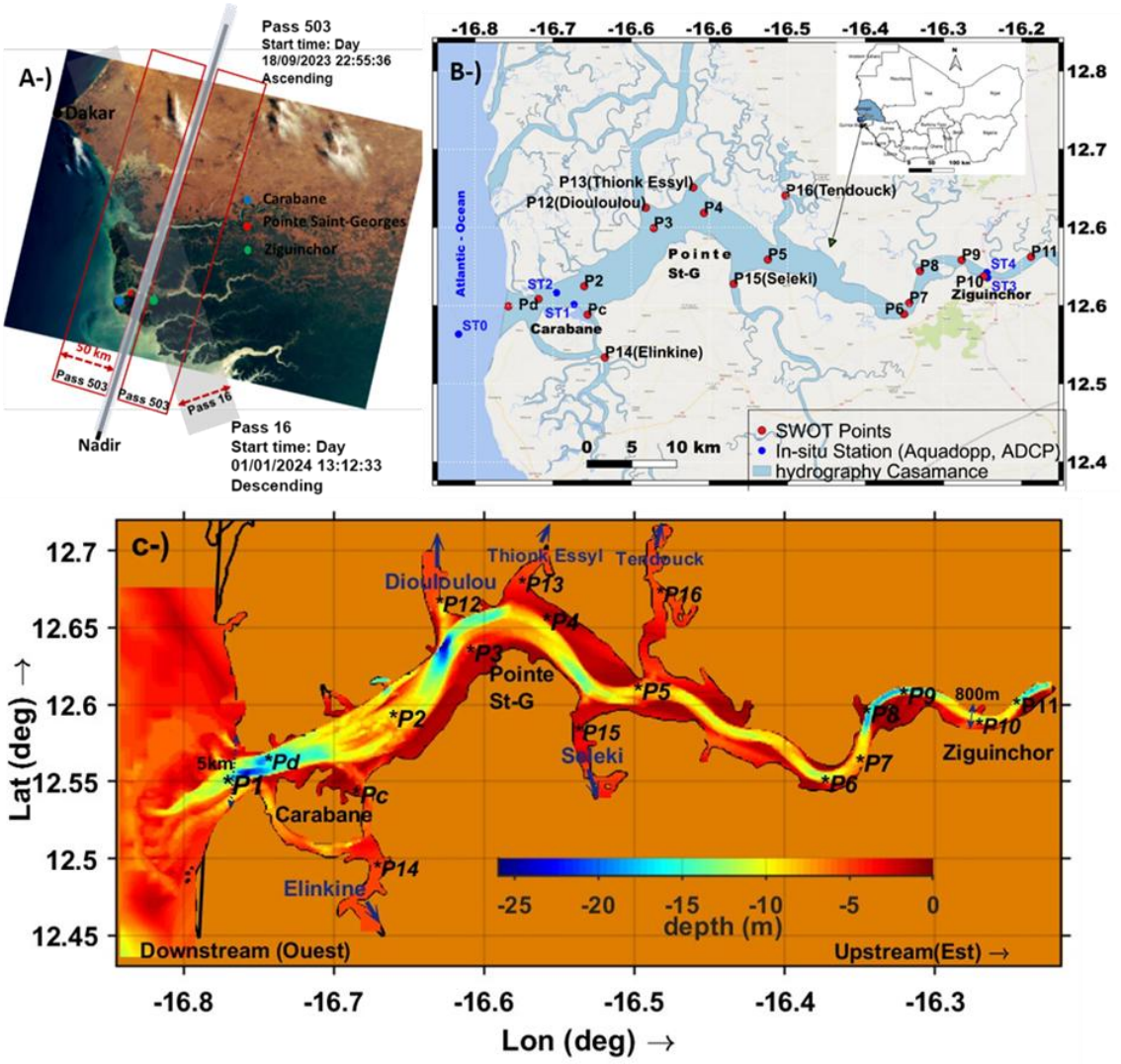

Figure 1. Study area: Casamance estuary (Senegal). A-) Upward (pass 503) and downward (pass 16) trajectories of the SWOT satellite over the study area on September 18, 2023.B-) Location of SWOT points (red) and in-situ (blue) stations for measuring water level, current velocity (AWAC ADCP) and bathymetry in the Casamance estuary. C-) Interpolated bathymetry on the structured grid of the Delft3D model with a spatial resolution of 124 m. The arrows indicate the direction of the main current in the estuary, with upstream (east) on the right and downstream (west) on the left. The names of the major localities (Carabane Island downstream, Pointe Sain-Géorges) are indicated as spatial landmarks.

2.2. In-Situ Data

In order to analyse the hydrodynamic dynamics of the Casamance estuary, several measurement campaigns were conducted using AWAC ADCP instruments (in 2012 and 2021) and Aquadopp sensors (in 2023). These instruments were deployed at multiple locations and depths, enabling the collection of time series data on current velocity and water level with varying temporal resolutions (Table A1).

The Aquadopp sensors recorded data at 30-second intervals, which were subsequently averaged over 10-minute periods for analysis. In addition, the Aquadopp sensors installed at the Carabane and Ziguinchor pontoons record time series data to characterise the tidal signal both upstream and downstream of the estuary (Figure 1).

The AWAC ADCP estimates water velocity by measuring the Doppler shift of the reflected acoustic signal. It samples the water column in cells of 50 cm in height, measuring current speed and direction within each of the 8 to 12 vertical cells. Tidal information was also obtained via the internal pressure sensor. Current and tidal data were averaged over 60-second periods and recorded every

 doi:10.20944/preprints202507.2525.v1

15 minutes. The AWAC ADCPs, which provide information throughout the water column, allow for the analysis of vertical circulation and the validation of hydrodynamic simulations using Delft3D. Measurements taken at the estuary mouth and within the Carabane channel offer a detailed view of current structures as a function of depth.

A Teledyne RDI ADCP was installed on the pole of the "Vedette" boat to measure current speed and direction throughout the water column while navigating. Transects in upstream and downstream were surveyed during both neap and spring tides. Each transect was sailed back and forth at low speed (1–2 m/s), over the course of a day (or less), in order to accurately capture current variations. These measurements were used to quantify the flow rate across each section during specific tidal phases.

2.3. TPOX8 Tidal Model

The TPXO8 model represents the eighth iteration of the TPXO global barotropic tidal model, which was developed by Oregon State University [57,58]. The model is based on the solution of depth-averaged shallow water equations under the barotropic assumption, neglecting internal density variations. The model assimilates a comprehensive set of satellite altimeter data from missions such as TOPEX/Poseidon, Jason-1 and -2, Envisat, and ERS-2, thereby enabling the accurate global estimation of the major tidal constituents [59].

TPXO8 provides amplitudes and phases for up to 13 tidal constituents, including M2, S2, K1, O1, N2, and others, on a global grid with a horizontal resolution of 1/30° (~4 km). A significant advantage of the proposed approach is its capacity for assimilating satellite observations to rectify modelled tides, thereby enhancing the precision of tidal predictions across both deep oceanic regions and coastal zones [60].

Several studies have validated the performance of TPXO models in various environments, including estuaries, shelf seas, and open oceans, making TPXO8 a widely accepted source for tidal boundary conditions in coastal and estuarine hydrodynamic modelling [61–63].

2.4. Delft3D Hydrodynamic Modeling

2.4.1. Model Configuration

Version 4.04.02 of the Delft3D-FLOW module is used to model flow dynamics in the Casamance estuary by incorporating complex hydro-morphodynamic processes. This open-source model solves the three-dimensional Navier–Stokes equations for incompressible flow under the Boussinesq approximation, employing a k–ε turbulence closure scheme to estimate turbulent kinetic energy and its dissipation [64–72].

The domain is discretised using a structured curvilinear grid generated with RGFGRID [73] (Deltares, 2024), comprising 559 longitudinal and 253 transverse cells. This grid resolution offers a robust compromise between numerical accuracy and computational efficiency. The model uses an Arakawa C-grid to enhance the accuracy of velocity and water level gradients [66,67,73].

The modelled domain spans approximately 70 km—from ~5 km upstream of Carabane to ~5 km downstream of Ziguinchor—and is solved using a finite volume approach. Water levels and scalar concentrations are defined at cell centres, while horizontal velocity components are calculated on the cell edges (Figure 1).

In the Casamance estuary, the flow regime is fluvial and subcritical, with a Froude number (Fr) < 1, justifying the use of the hydrostatic assumption. Due to the weak vertical stratification [50], a σ-layer vertical discretisation is adopted, providing improved representation of bathymetric variations [67,74].

The bathymetric dataset used in this study is derived from hydrographic surveys conducted using single-beam echosounders: Reson Navisound (210 kHz) and Odom Hydrotrack (200 kHz). Measurements were acquired along transects spaced at 400 m intervals, reduced to 200 m in the vicinity of the estuary mouth to enhance spatial resolution. Additionally, a dedicated high-resolution

 doi:10.20944/preprints202507.2525.v1

survey was carried out around Carabane Island [75]. To complement these in situ measurements and adequately represent the offshore boundary conditions, bathymetric data from the GEBCO 2023 global dataset were incorporated to characterise the estuary's opening to the Atlantic Ocean. The combined dataset was interpolated onto the model grid, which has a spatial resolution of 124 m, using the QUICKIN module in Delft3D [76], ensuring a consistent and continuous bathymetric surface across the entire modelling domain.

2.4.2. Tidal Boundary Conditions

Tidal forcing at the open ocean boundary of the model domain was derived from the global barotropic model TPXO8, developed by Oregon State University [77]. This model solves the depth-integrated shallow water equations and assimilates satellite altimetry data from missions such as TOPEX/Poseidon, Jason-1/2, Envisat, and ERS-2 to improve accuracy, particularly in coastal and shelf regions [59].

The TPXO8-atlas version offers an enhanced horizontal resolution of ~1/30° to 1/60° (2–4 km), enabling a finer representation of tidal gradients in complex coastal and estuarine environments. It provides amplitudes and phases for 13 tidal constituents, including the dominant semi-diurnal (M2, S2, N2) and diurnal (K1, O1, P1, Q1) components relevant for the Casamance estuary [47,49,50]. Nonlinear constituents such as M4 and MS4 often amplified upstream are also included and reflect tidal distortion processes linked to the generation of overtides, which are crucial for understanding extreme water level variability [49]. Long-period constituents (Mm, Mf, MN4) are present but have a minor effect in this regional context.

In this study, the main constituents were extracted from the TPXO8 dataset and applied at the boundary using harmonic synthesis. This approach ensures realistic tidal wave propagation into the estuary and supports the simulation of key dynamics such as water level variability, tidal asymmetry, and the interaction between diurnal and semi-diurnal components. While TPXO8 performs well in open ocean and coastal settings, its limited resolution and lack of local forcing (e.g., bathymetry, river discharge) may reduce accuracy in narrow or shallow estuarine zones.

2.4.3. Turbulence Modeling and Vertical Flow Structure

In Delft3D-FLOW, turbulence is modelled using a scheme in which the turbulent kinetic energy (k) and its dissipation rate (ε) are determined through transport equations [67,78]. The turbulent viscosity is defined by the expression $\nu_t = C\mu\, L\sqrt{k}$, where Cμ is a calibration constant and L is the mixing length, itself derived from an empirical formulation based on a specific calibration coefficient. The initial state is characterised by a prescribed viscosity and diffusivity of 1×10^{-6} m²/s. Boundary conditions vary depending on the type of boundary. Along closed boundaries, the normal velocity component is set to zero, and a friction coefficient of 0.08 is applied to adjust the shear stresses. At the bottom and at the free surface, vertical velocity is set to zero. At the bed, the shear stress is calculated by considering wave–current interactions, using the formulation $\tau_b = \tau_c + \tau_w$, where τ_c and τ_w represent the shear stresses induced by currents and waves, respectively. Across the entire model domain, a Manning roughness coefficient ranging between 0.022 and 0.024 is employed to simulate bed friction. At open boundaries, conditions are specified according to location. At the seaward boundary, as well as upstream at Ziguinchor and the tributaries on both the left and right banks, water level and sediment concentration are imposed as zero (wl = 0, Cs = 0). The model accounts for three types of sediment, all defined by a reference density of 1600 kg/m³ and differing particle sizes: coarse sand (D_{50} = 0.457 mm), fine sand (D_{50} = 0.1 mm), and silt (D_{50} = 0.04mm). These grain sizes were selected based on the work of [55,56] in the estuary and Diatta (2024) on the intertidal flats of Diogué and Carabane.

2.5. SWOT Observation

 doi:10.20944/preprints202507.2525.v1

2.5.1. SWOT L2_HR_PIXC Product Overview

The SWOT (Surface Water and Ocean Topography) satellite, developed by NASA and CNES with the support of CSA and UKSA, was launched on 16 December 2022. It operates in a non-sun-synchronous orbit (with an inclination of 77.6° and an altitude of 890.6 km), and its scientific phase cycle is 21 days [79].

The primary instrument employed is the Ka-band Radar Interferometer (KaRIn), which utilises a bistatic Ka-band radar configuration operating at a frequency of 35.75 GHz, with a wavelength of 8.4 mm. The apparatus is supported by a 10-meter pole to which are affixed two antennas, the purpose of which is to provide a reduced angle of incidence (40.65° to 43.9°) for the purpose of accurate water level measurements. It is imperative to note that a nadir altimeter is essential for ensuring the continuity of observations over a distance of 20 km [38,79–81].

KaRIn collects data over two 50 km the nadir. SWOT is also equipped with a Nadir altimeter (Poseidon-3C) providing measurements within the 20 km gap between KaRIn swaths. The system is designed to measure Sea Surface Height (SSH) in the ocean with a resolution of 1 km × 1 km, and to measure water surface elevation over terrestrial water reservoirs , including rivers (wider than >100 m), lakes (larger than >250 m × 250 m) and wetlands. The system's accuracy has been documented as 10 cm in water height and 1.7 cm/km for slopes on water bodies with a minimum area of 1 km².

In this study, the L2_HR_PIXC (Level 2 High Rate Pixel Cloud) product is utilised to analyse hydrological and estuarine dynamics (Figure 2). Derived from the KaRIn interferometer aboard the SWOT mission, this product delivers high-resolution observations of surface water extent and elevation over water bodies typically wider than 50–100 metres. The data are organised as pixel clouds for each half-swath (left or right) within a tile of approximately 64 × 64 km² and are distributed in netCDF-4 format. Each pixel includes geolocated water surface elevation, backscatter information, geometric parameters such as width, slope, and area, as well as quality flags and uncertainty estimates. Spatial resolution ranges from 5 to 100 metres, depending on surface characteristics and observation conditions, enabling the detection of fine-scale spatial patterns in surface water dynamics.

The utilisation of SWOT signifies a substantial advancement in surface water monitoring, particularly in microtidal tropical estuaries such as the Casamance. Its capacity to furnish uninterrupted, two-dimensional elevation data at elevated spatial resolution fosters enhanced quantification of water level and reinforces the calibration and validation of hydrodynamic models [79,82–84].

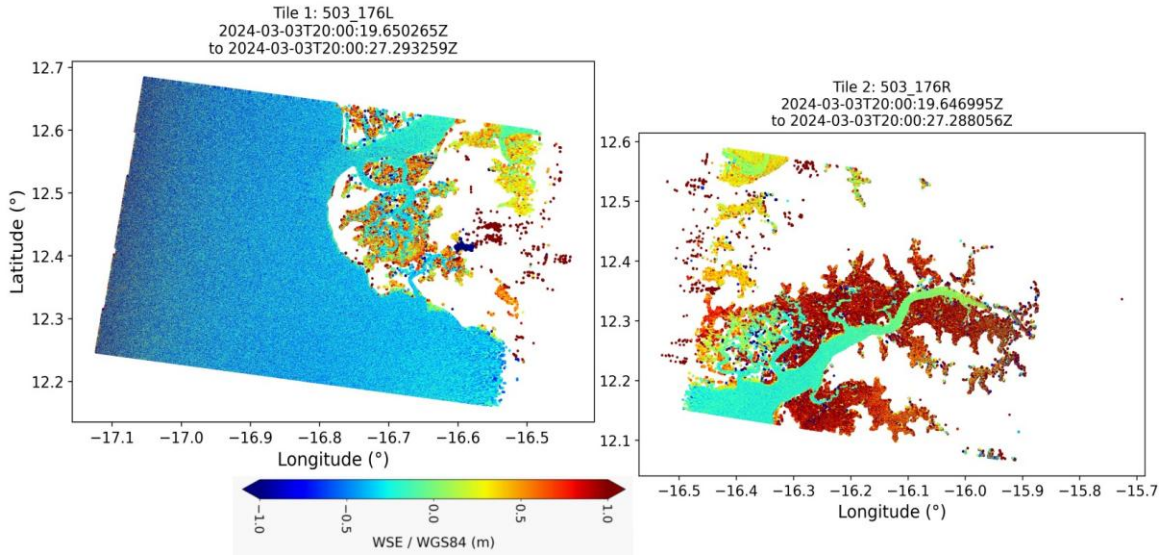

Figure 2. Illustration of the L2_HR_PIXC (High Resolution Pixel Cloud) product during the 503 cycle of pass 176, showing two tiles: Track R (to the right of the nadir) and Track L (to the left of the nadir).

 doi:10.20944/preprints202507.2525.v1

2.5.2. Extraction of water Levels and Estimation of Hydraulic Slopes

The characterisation of water levels is achieved through the utilisation of the Water Surface Elevation (WSE) parameter, which is defined with respect to the WGS84 ellipsoid. The SWOT slope is calculated according to the methodology of the SWOT team [83], by applying the geoid and tidal corrections to the heights of the pixels relative to the ellipsoid (see Equation 1).For each pass, the corrected water heights are spatially aggregated by selecting the pixels located within a radius of 200 m around the N station. The weighted average of these values provides a representative estimate of the water level at the station (Equation 2).

$$\boldsymbol{h(x) = H(x) - geoid_{hight(x)}} \quad (1)$$

$\boldsymbol{h(x)}$: Water Surface Elevation (WSE) for pixel x.

H(x): Pixel height measured relative to the WGS84 reference ellipsoid.

$\boldsymbol{geoid_{hight(x)}}$: Height of the geoid (correction for the actual shape of the Earth).

$$\mathbf{h_n = \frac{\sum_{x \in R} h(x)}{N}} \quad (2)$$

$\boldsymbol{h_n}$: average water level at the station.

$\boldsymbol{h(x)}$: WSE corrected for pixel x.

R: All SWOT pixels located within a radius of 200 m around the station.

The longitudinal slope of the free surface is evaluated from the WSE values extracted at different stations located between P1, downstream, and P11, upstream (Figure 1). These stations are positioned in the center of the main flow channel, thus allowing a detailed analysis of the hydrodynamic variations along the estuary.

The Figure 3 illustrates the simulated water levels produced by Delft3D-Flow in comparison with the observed data from the SWOT mission. Tide gauge stations P10 (upstream) and P2 (downstream) were utilised for model calibration and validation over the period from January to March 2023. The tidal signal, represented by the light grey area, illustrates the simulated water levels, highlighting a semi-diurnal cycle with amplitude variations characteristic of spring tides and neap tides. The SWOT passages are indicative of the irregular distribution of the satellite's scientific orbit above the two stations.

In the upstream area of the estuary (panel a), SWOT observations encompass a broad spectrum of tidal conditions, predominantly at mid-levels, with sporadic occurrences in proximity to MHWS (Mean High Water Springs) and MLWS (Mean Low Water Springs). In the downstream region (panel b), the SWOT passages are distributed uniformly across all tidal heights. The comparison between P10 and P2 highlights discrepancies in amplitude, which is indicative of disparate estuarine dynamics. The ability of SWOT to represent hydrodynamic variations within the estuary is contingent on an understanding of these contrasts.

The instantaneous water discharge is estimated at two cross-sections using a height–fall–discharge (HFD) relationship derived from the empirical Manning–Strickler equation (Equation.3). This approach has been successfully applied in various estuarine and tidal river environments to estimate total flow within the fluvial system [83].

Equation (2) is applied to distinct sections of the estuary. The downstream cross-section, located at the mouth, is the widest (~4 km), whereas the upstream section is approximately 800 m wide. The hydraulic parameters, particularly the wetted area A_w (in m²) and wetted perimeter P_w (in m), are derived from bathymetric soundings and water surface elevations provided by SWOT. The hydraulic slope S is calculated for each section and for each SWOT pass, using Equation (4). The sign of the slope, sign(S) is assigned based on the direction of the hydraulic gradient: +1 during flood (rising tide) and -1 during ebb (falling tide).

$$\mathbf{Q(t) = Sign(S).K.A_w Z(t).R_h(Z(t))^{2/3}\sqrt{S(t+\Delta t)}} \quad (3)$$

$$\mathbf{Z(t) = Z_{swot}(t)} \quad (4)$$

$$\boldsymbol{S_0 \frac{h_n - h_0}{L_w}} \quad (5)$$

Q is the flow rate (in m³/s),

K is the Manning–Strickler coefficient (in $\boldsymbol{m^{1/3}/s}$), K=10, 15, 20 ...

 doi:10.20944/preprints202507.2525.v1

A_w is the cross-section of the river (in m²),

R_h is the hydraulic radius (in m),), $R_h = A_w / P_w$

h_0 and h_n represent the SWOT-derived water surface elevations at the downstream (right bank) and upstream (left bank) ends of the estuarine reach, respectively. For the calculation of the longitudinal slope of the estuary, h_0 corresponds to the water level at the mouth (downstream), while h_n corresponds to the water level upstream.

L_w refers to the width of the estuary cross-section, or alternatively to the length of the estuarine reach, depending on the context (i.e., whether used in transversal or longitudinal slope estimation).

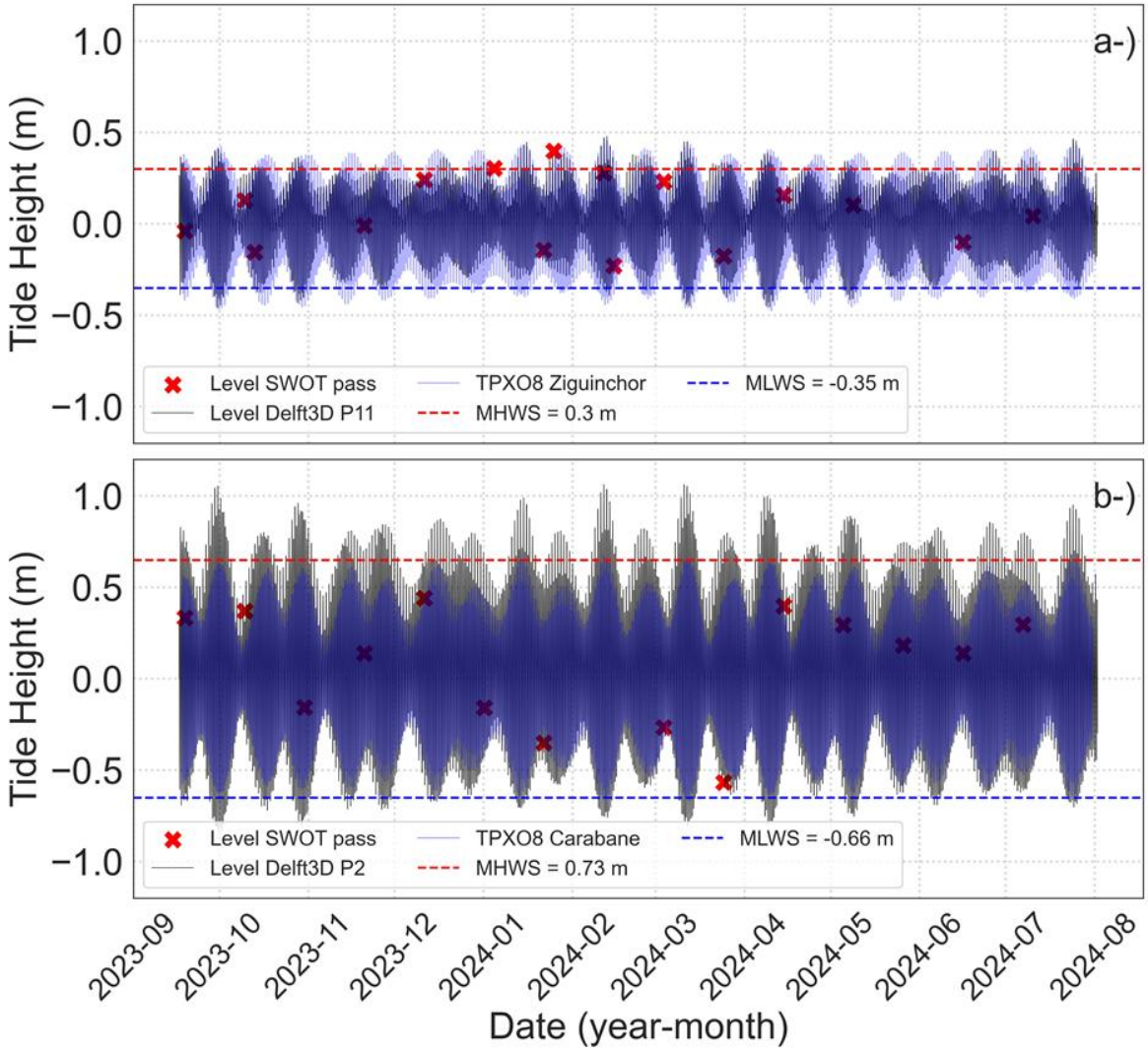

Figure 3. Illustration of the time series of the hydro-morphodynamic model data, the upstream (a) and downstream (b) TPXO8 and SWOT data.

3. Results

3.1. Validation of the Delft3D-Flow Hydrodynamic Model

Figure 4 compares the observations and simulations of the hydrodynamic model in terms of water levels and vertical current structure at the Carabane and Ziguinchor stations. The model (A) reproduces the vertical structure of the currents observed (B) upstream and downstream. In November, the estuary is relatively well mixed, with low contrast at the mouth, indicating a low density gradient or signal disturbance by fine solid particles in this area of the estuary. A residual current directed towards the sea is also present, more marked at the mouth.

 doi:10.20944/preprints202507.2525.v1

The central graphs validate the model's simulation of water levels compared to observations on a semi-diurnal tidal cycle. At Carabane, the model faithfully follows the temporal variability of the tide, with an RMSE of 0.079 m, an MAE of 0.065 m, a coefficient of determination R^2 of 0.906 and a Pearson correlation of 0.995. In Ziguinchor, although performance remains satisfactory, it is slightly degraded, with an RMSE of 0.084 m, an MAE of 0.065 m, an R^2 of 0.719 and a Pearson correlation of 0.961

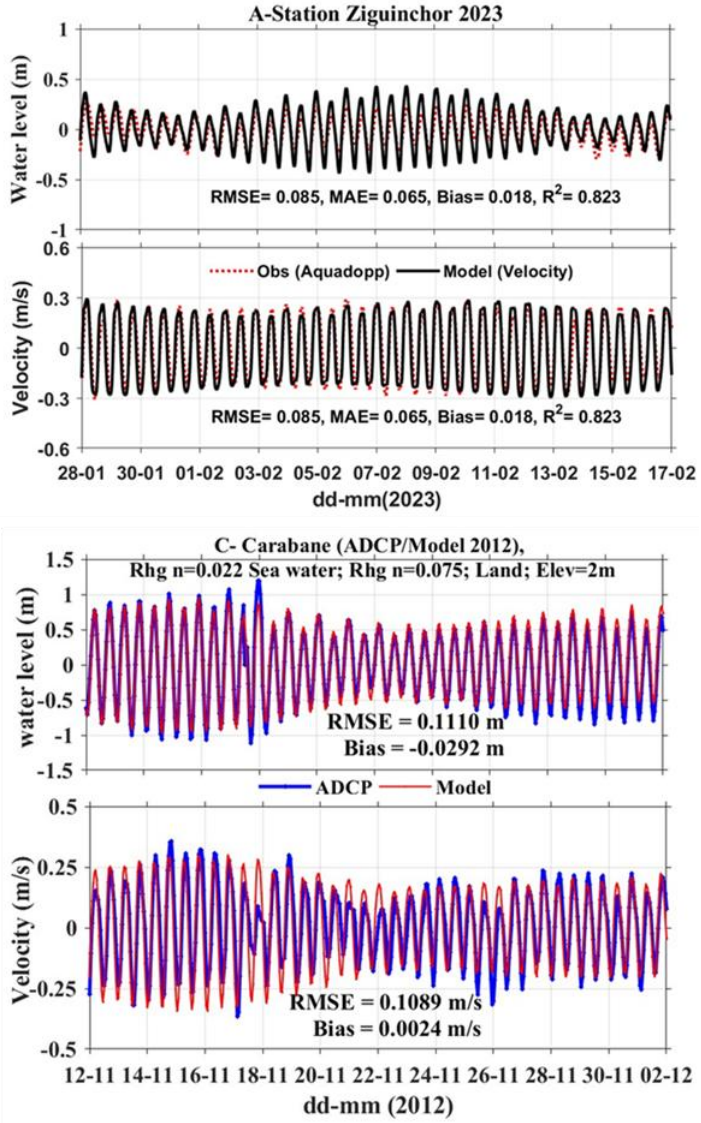

Figure 4. Validation du modèle hydrodynamique : comparaison des niveaux d'eau et des vitesses courantes observées et modélisées à la station Offshore (5 km de Carabane, AWAC ADCP à 6 m) et à la station de Ziguinchor (3 m sur la rive droite de l'estuaire).

3.2. Validation of the Vertical Structure of the Delft3D-Flow Hydrodynamic Model

Figure 5 compares observations with the Delft3D hydrodynamic model results regarding water levels and the vertical current structure at the Carabane and Ziguinchor stations. Panel A shows that the model successfully reproduces the vertical structure of currents observed in Panel B, both upstream and downstream. In November, the estuary is relatively well mixed, with little contrast in the vertical structure at the mouth. This suggests either a weak density gradient or a disturbance caused by suspended fine particles. A residual current directed seawards is present and more pronounced at the mouth.

 doi:10.20944/preprints202507.2525.v1

The central plots illustrate the comparison between simulated and observed water levels over a semi-diurnal tidal cycle. At Carabane, the model closely follows the tidal signal with strong performance metrics (RMSE = 0.079 m, MAE = 0.065 m, R^2 = 0.906, Pearson correlation = 0.995). At Ziguinchor, the agreement remains satisfactory but is slightly reduced (RMSE = 0.084 m, MAE = 0.065 m, R^2 = 0.719, Pearson correlation = 0.961).

The vertical profiles of tidal currents at both stations confirm the model's capacity to reproduce the tidal phases. The simulated currents accurately reflect the measured structure, including flow reversals and locations of maximum velocities. The residual currents (shown in red), computed between flood and ebb, exhibit a marked asymmetry, highlighting the role of tidal distortion in shaping residual circulation in the estuary.

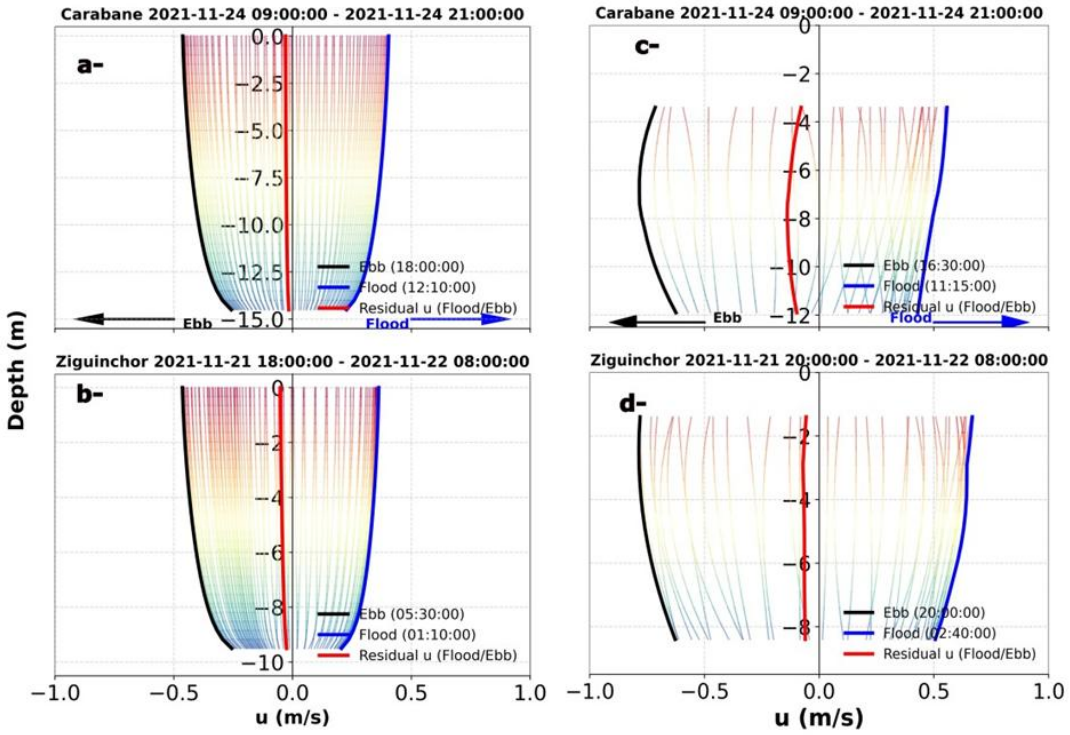

Figure 5. Validation of the hydrodynamic model by comparison of the vertical current profiles at the Carabane (depth ~14 m) and Ziguinchor (depth ~9 m) stations. The first column (a, b) shows the currents recorded by the AWAC ADCP, measured in 50 cm thick cells, while the second column (c, d) presents the currents simulated by the model, distributed over 30 vertical levels. The black and blue curves show the average profiles during the ebb (Ebb) and flood slack periods, respectively. The red curve represents the residual velocity (Flood – Ebb).

The results of section 2.2 confirm the ability of the model to reproduce the tidal dynamics and the horizontal circulation in the estuary. However, there are slight discrepancies, particularly in current velocities. The results of paragraph 2.3 show that the model is able to accurately reproduce the dynamics of the currents and the vertical structure of the circulation in the Casamance estuary, emphasising a more pronounced ebb/flow residual current directed towards the sea.

3.3. Validation of the Vertical Structure of the Delft3D-Flow Hydrodynamic Model

Figure 6 show comparison between the water levels observed by SWOT and simulated by Delft3D demonstrates a high degree of agreement along the primary channel (stations P1 to P11), with correlation coefficients exceeding 0.80 and regression slopes approaching 1. Downstream (station P1), the correlation reaches R= 0.804 with a slope of 0.99, while upstream, near Ziguinchor (P11), the correlation remains strong (R= 0.837), but the slope decreases to 0.61, reflecting a progressive underestimation of the simulated levels. The intermediate stations (P2 to P9) substantiate

 doi:10.20944/preprints202507.2525.v1

this trend, with RMSE generally less than 0.15 m and no significant trend detected (Mann-Kendall test, $p > 0.05$) (see Table 1). In contrast, the performance of the model deteriorates in the tributaries (stations P12 to P16). The correlations in these areas are lower (R ranging from 0.42 to 0.74), the slopes deviate by 1 (between 0.60 and 1.10), and the errors increase to 0.339 m at station P12.

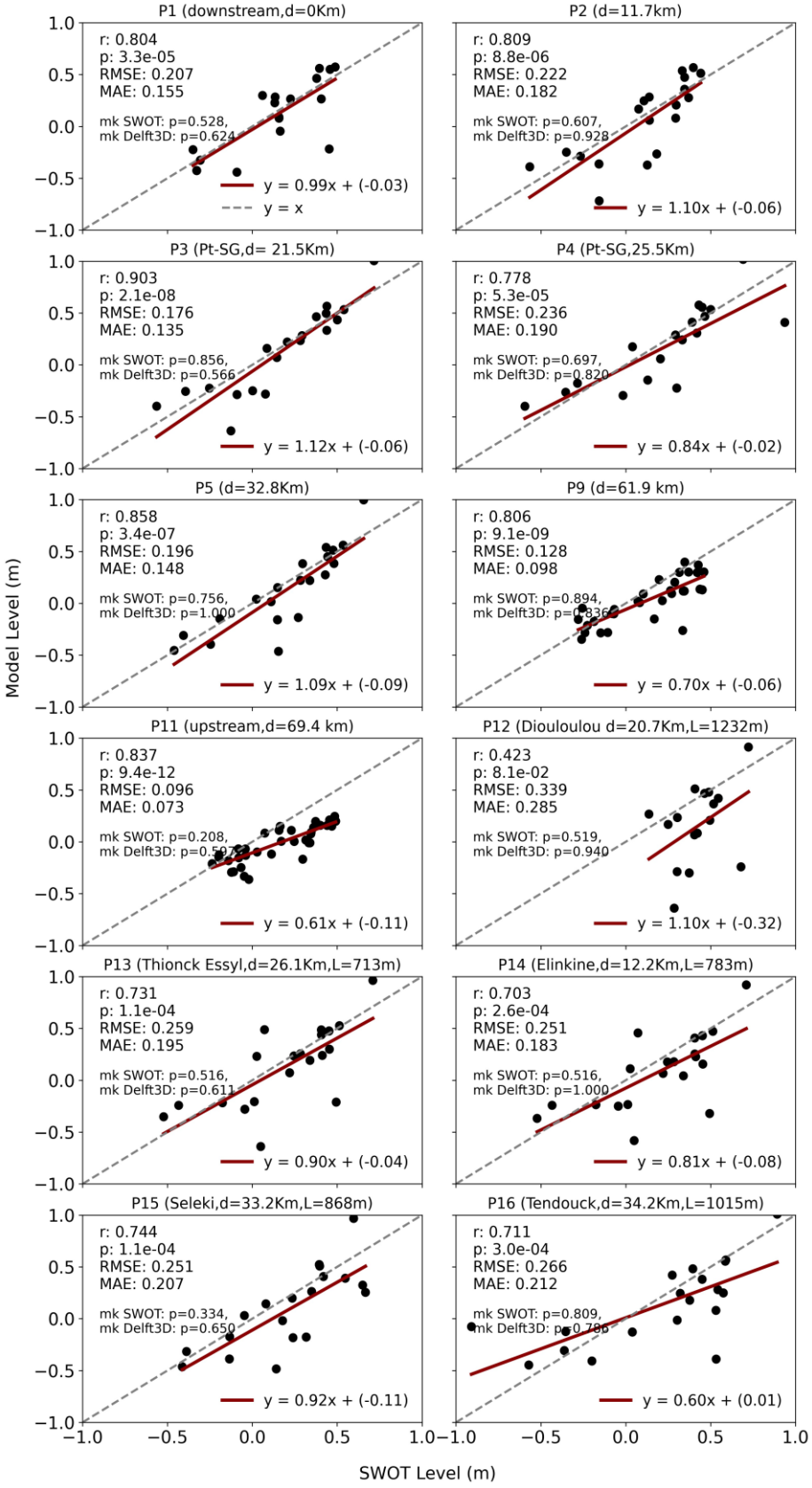

Figure 6. Comparison of water levels simulated by the Delft3D-Flow model and SWOT observations.

 doi:10.20944/preprints202507.2525.v1

Figure 7 provides an overview of the comparison between SWOT observations and Delft3D simulations in the Casamance estuary. The model performs well in the main channel (stations P1 to P11), with high correlation coefficients (up to 0.90) and low errors (RMSE < 0.25 m), which can be attributed to accurate bathymetric data in this area. In contrast, the performance drops significantly in the tributaries (stations P12 to P16), where correlation decreases (as low as 0.42) and RMSE increases (up to 0.34 m), likely due to interpolated bathymetry and more complex local hydrodynamics. These results highlight the critical role of bathymetric data quality in achieving reliable hydrodynamic simulations.

Table 1. Statistical summary of the comparison between SWOT and Delft3D.

Station	Correlation (R)	Slope	SWOT trend	Delft3D trend	Interpretation
P1 (downstream)	0.804	0.99	NS	NS	Good agreement between observed and simulated water levels
P11 (upstream, 70km)	0.837	0.61	NS	NS	Underestimation of amplitude in the model
P12–P16 (tributaries)	0.42–0.74	0.60–1.10	NS	NS	Weak signal; model performance requires improvement
P2–P9 (main channel)	> 0.80	~1.0	Mixed (often NS)	NS to strongly stable	Good alignment; little to no trend observed

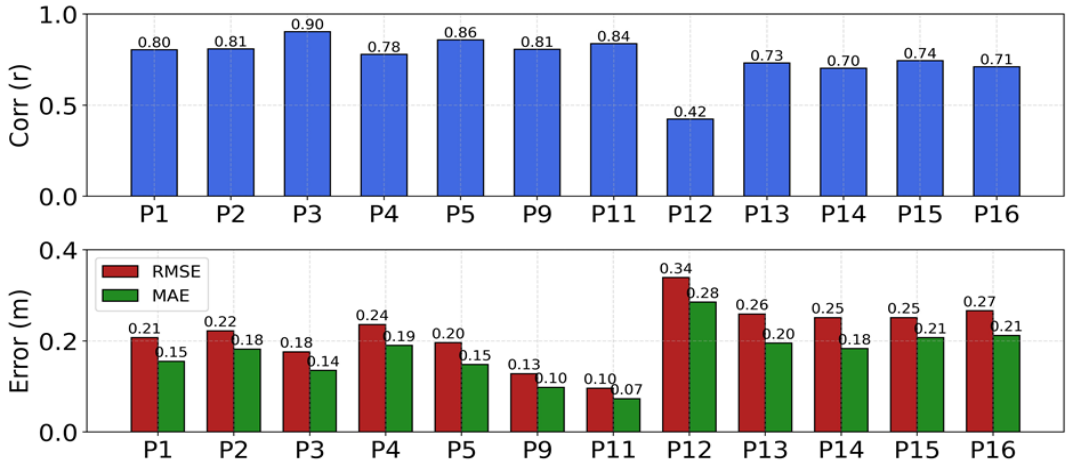

Figure 7. Comparison of SWOT data and Delft3D simulations in the Casamance estuary. This figure shows the performance of the Delft3D model compared to SWOT observations at different points in the Casamance estuary.

Figure 8 shows the comparison between water levels simulated by the Delft3D numerical model (top), TPXO8 data (bottom), and SWOT satellite observations at two stations in the Casamance estuary: Diogué, located 4.5 km from the Atlantic Ocean at the downstream end of the estuary, and Carabane, situated further upstream at 9.3 km. Each plot includes a regression line between observed levels (SWOT, x-axis) and simulated levels (y-axis), along with the identity line y = x. Standard performance metrics are also provided: Pearson correlation coefficient (r), coefficient of determination (R^2), root mean square error (RMSE), mean absolute error (MAE), and the linear regression equation.

At Diogué, Delft3D shows the highest performance, with a correlation coefficient of R= 0.877, a regression slope of 1.10, an RMSE of 0.204 m, and an MAE of 0.167 m. TPXO8 also performs well at this station (R= 0.853, slope = 0.93, RMSE = 0.193 m, MAE = 0.167 m). At Carabane, Delft3D maintains good agreement (R= 0.843, slope = 1.11, RMSE = 0.225 m), while TPXO8 shows reduced performance

 doi:10.20944/preprints202507.2525.v1

(R= 0.776, slope = 0.77, RMSE = 0.198 m). These results indicate that Delft3D, with its finer spatial resolution, captures more effectively local hydrodynamics near the estuary mouth, whereas TPXO8, designed for larger-scale applications, is less adapted to these areas.

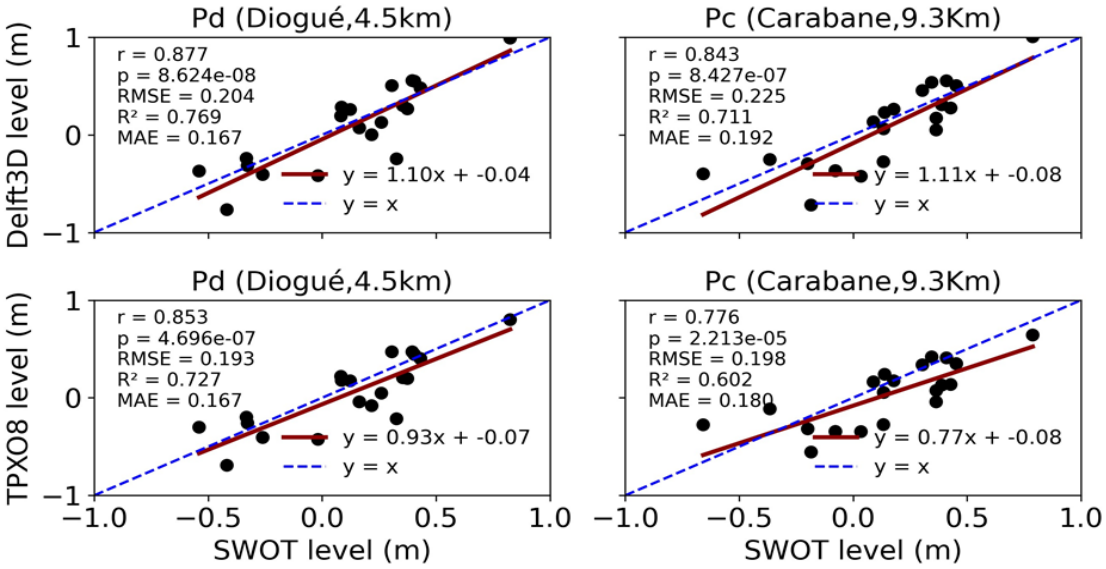

Figure 8. Comparison of water levels simulated by the Delft3D-Flow and TPXO8 flow model with SWOT observations at Diogué (4.5 km from the ocean) and Carabane (9.3 km) upstream of the Casamance estuary.

Figure 9 compares flow rate measurements obtained by the Teledyne AWAC ADCP and those estimated by SWOT in the upstream (S8) and downstream (S1) sections of the Casamance River. SWOT effectively captures the estuary's overall flow regime, with higher volumes at the mouth and a significant decrease upstream, where only about 15% of the downstream volume is recorded at Ziguinchor for each tidal phase.

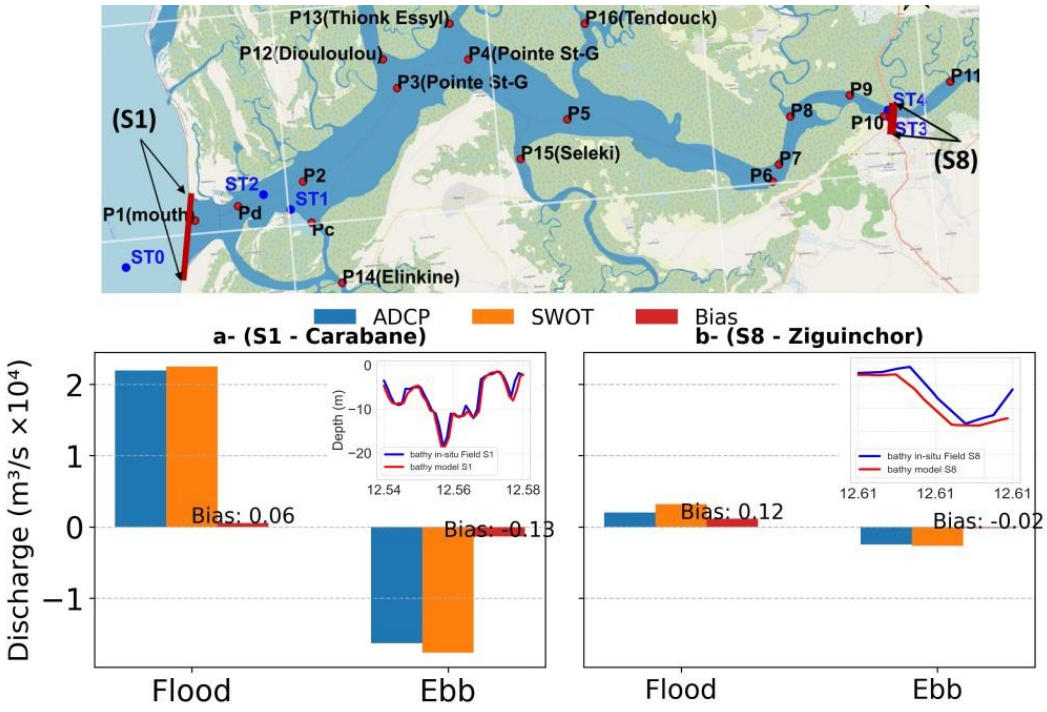

Figure 9. Comparison of discharge estimates from SWOT and Teledyne RDI ADCP measurements at two cross-sections in the Casamance estuary: (a) S1 – Carabane (4 km wide) and (b) S8 – Ziguinchor (700 m wide), during

 doi:10.20944/preprints202507.2525.v1

flood and ebb phases. Bias values are indicated for each tidal phase. Insets show cross-sectional bathymetric profiles, with in-situ data in blue and modelled bathymetry in red.

However, SWOT tends to overestimate flow rates, particularly during the flood phase, with a more pronounced bias in the upstream section. This overestimation becomes more evident with rising water levels, especially near the mouth (see Figures 9a and 9b). Despite these discrepancies, SWOT provides acceptable estimates of flow, although its accuracy varies depending on the tidal phase.

The overestimation is likely due to SWOT's wide spatial footprint, which captures a larger flow section than the Teledyne RDI ADCP, whose measurements are limited by shallow waters and complex environments near banks and mangroves. As a result, SWOT integrates broader cross-sections, leading to inflated flow estimates relative to the more localised ADCP data.

3.4. Analysis of the Spatial Variation of Current Velocities in the Casamance Estuary

3.4.1. Analysis of the Spatial Variation of Current Velocities in the Casamance Estuary

Figure 10 illustrates the spatial distribution of current velocities in the Casamance estuary across different tidal phases, based on hydrodynamic model results. The model successfully reproduces peak flow patterns and the reversal of tidal currents between flood and ebb phases under both spring and neap tide conditions.

During the spring tide flood (21 February 2023, 09:00), incoming tidal flows reach up to 1 m/s, particularly in the main channel near the mouth and around Carabane. This velocity increase is attributed to channel constriction, which creates a throttling effect. During the ebb (same day at 16:00), seaward-directed flows dominate, also reaching 1 m/s, with intensified outflows between Carabane and Diogué. The model shows that ebb flows are generally stronger than flood flows in the lower estuary.

During neap tides (1 March 2023), current velocities are lower. Maximum speeds during both flood (04:00) and ebb (10:00) phases remain below 0.5 m/s. The circulation pattern remains similar to that of spring tides, although less energetic.

Strongest currents are consistently confined to the central channel, while the lateral margins exhibit slower velocities (0.2–0.3 m/s), due to shallow depths and recirculating flows. Zones like Pointe Saint-Georges and Elinkine act as energy buffers, favouring sediment deposition.

From the mouth to Pointe Saint-Georges, flow patterns are relatively symmetrical. However, near Ziguinchor, the asymmetry becomes more evident: flood velocities reach 0.4 m/s while ebb velocities drop to 0.2 m/s. Counter-currents develop along the banks, and the asymmetry is most pronounced during spring tides.

The analysis of current velocities in the open sea sector of the Casamance estuary highlights a time lag in flow propagation and a gradual attenuation of velocities along the estuarine axis (Figure 11). On 21 February 2023 at 23:00 UTC, near the mouth at Carabane, peak current speeds ranged from 0.3 to 0.5 m/s, reaching up to 0.6 m/s at Diogué and 0.7–0.8 m/s at Pointe Saint-Georges (Pt-SG). As the tidal wave moved upstream, velocities decreased to 0.2–0.3 m/s at Ziguinchor.

Three hours later, in Ziguinchor, the water level had dropped to 0.33 m, with velocities between 0.1 and 0.3 m/s, including quasi-stagnant zones, and around 0.2 m/s at Pt-SG. A counter-current developed along the right bank between Carabane and Pt-SG (9.5 km), with velocities ranging from −0.08 to −0.15 m/s at Carabane and reaching −0.4 to −0.5 m/s at Ziguinchor.

Flow propagation between Carabane and Ziguinchor showed a three-hour time lag, with average propagation velocities estimated at 0.3–0.4 m/s. These results indicate significant tidal energy dissipation due to bottom friction and the influence of local morphodynamics, resulting in marked current asymmetry.

At low tide slack, two distinct moments are observed: one at Carabane (21 February 2023, 17:00 UTC), and another at Ziguinchor (20:00 UTC), with a three-hour lag. At Carabane, the water level

 doi:10.20944/preprints202507.2525.v1

reaches −0.77 m. Residual currents in the main channel remain weak (< 0.2 m/s), while at Pt-SG they range from −0.4 to −0.6 m/s, and near the mouth from −0.5 to −0.7 m/s.

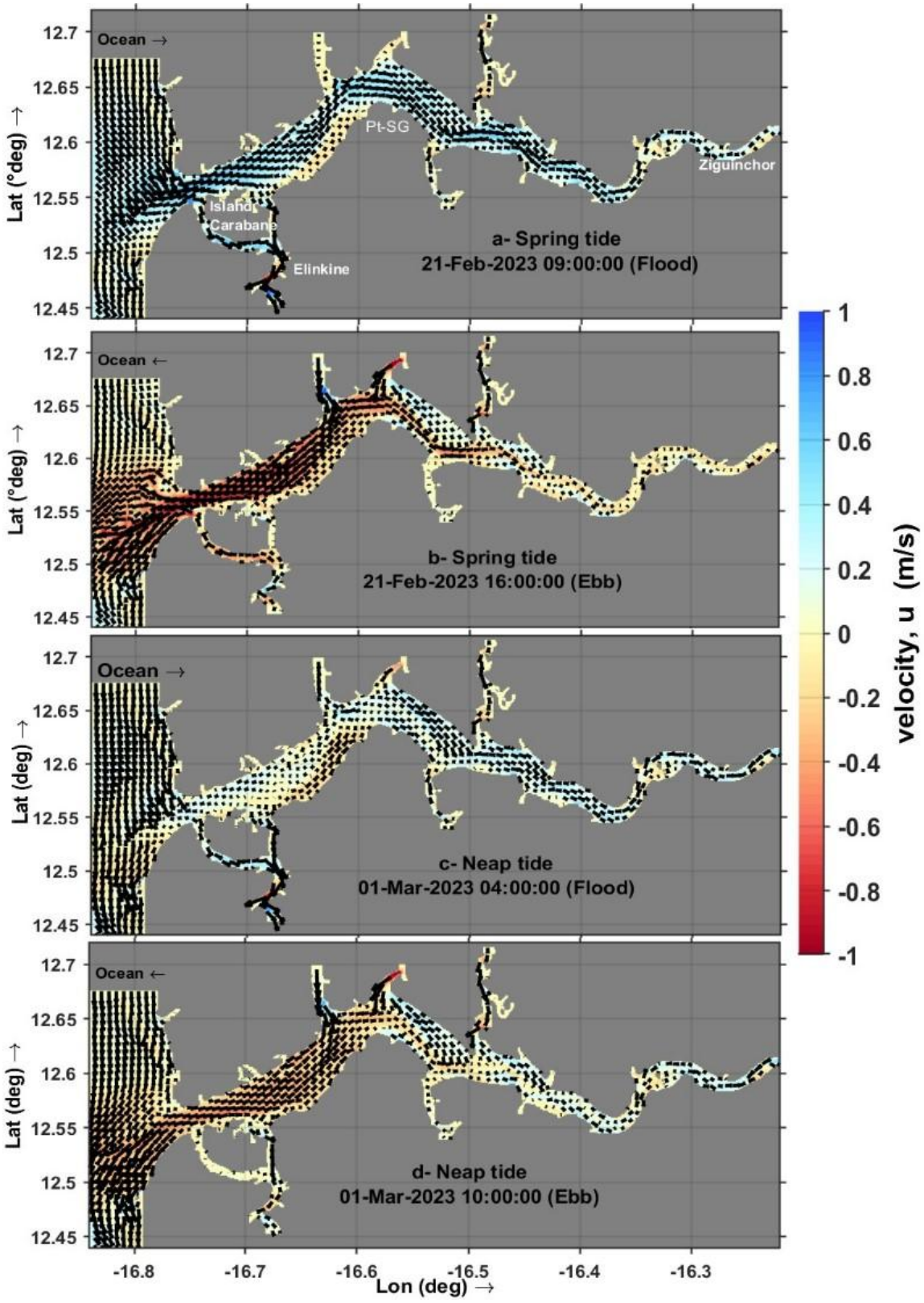

Figure 10. Spatial distribution of tidal horizontal current velocities in the Casamance estuary during flood and ebb phases, under spring and neap tide conditions.

 doi:10.20944/preprints202507.2525.v1

Three hours later in Ziguinchor, slack tide occurs at a higher water level (−0.35 m), with weak velocities (−0.1 to 0.2 m/s) across most of the estuary. Exceptions include Pt-SG (−0.3 to −0.4 m/s) and the mouth (−0.5 to −0.6 m/s).

During this slack phase, a counter-current forms along the estuarine banks: ~10 km along the left bank during the Carabane low tide, and ~9.5 km along the right bank during the Ziguinchor low tide, with velocities of −0.15 to −0.2 m/s. This spatial pattern of residual flow indicates lateral water storage and delayed return flows, contributing to tidal circulation asymmetry.

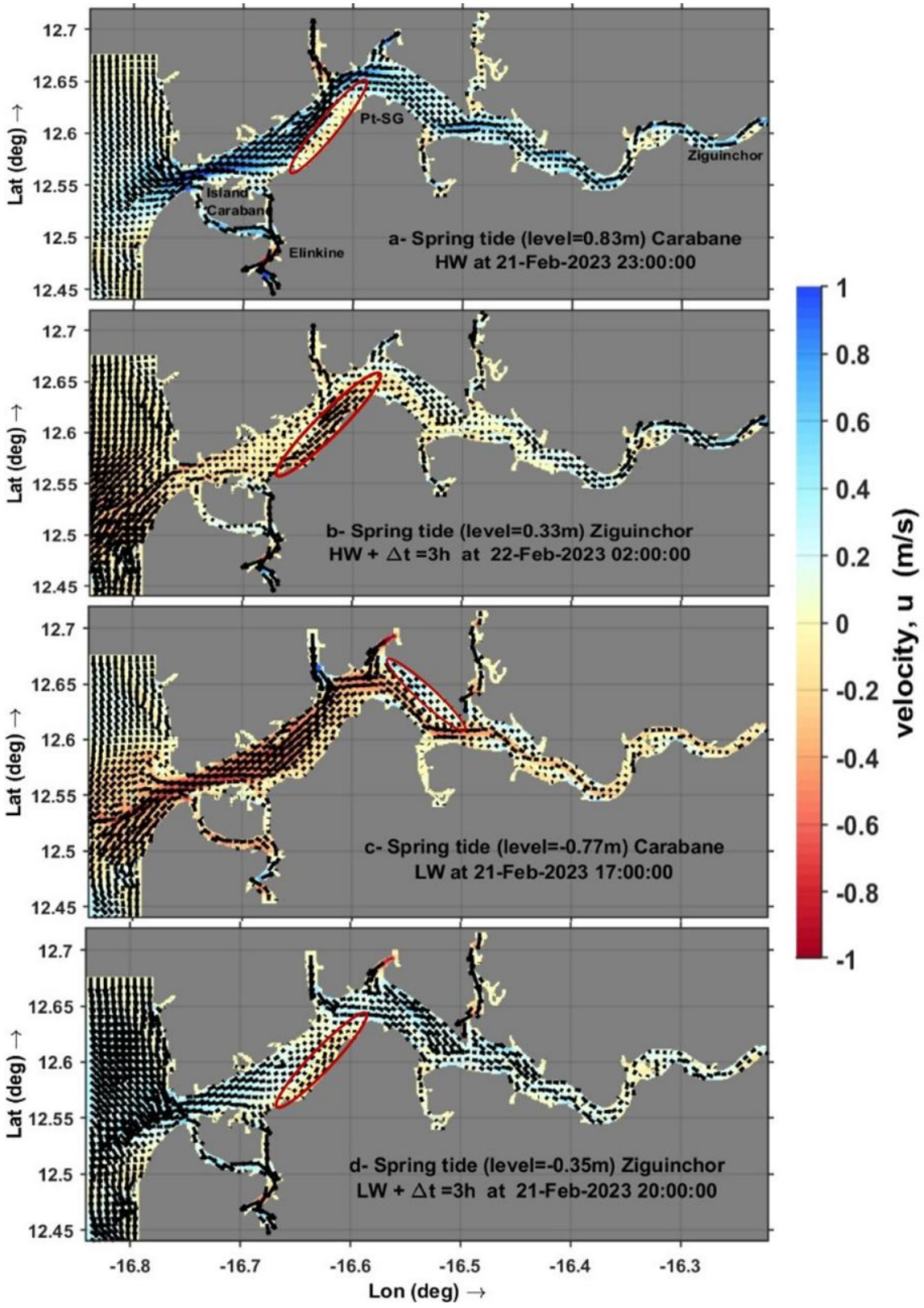

 doi:10.20944/preprints202507.2525.v1

Figure 11. Spatial distribution of tidal horizontal current velocities in the Casamance estuary during HW and LW, under spring and neap tide conditions.

3.5. Bottom Shear Stress and Sediment Transport in the Main Channel of the Estuary

A suite of morphodynamic sensitivity tests (MORFAC > 10, 10, 5, 2 and 1) was first performed to assess the impact of acceleration on channel evolution. Simulation outputs were then compared against high-resolution bathymetric surveys acquired at the estuary mouth and immediately adjacent to Carabane Island. While higher MORFAC values yielded exaggerated erosion and deposition zones—deviating markedly from the measured bottom elevations MORFAC = 1 produced a morphologic adjustment that most closely reproduced the surveyed bathymetry. Consequently, we focus our detailed comparison on two end-member runs (MORFAC = 10 and MORFAC = 1) in Figures X and Y, with MORFAC = 1 representing the optimal match to in situ bathymetry.

3.5.1. Situation MORFAC=10

Figure 12 highlights the sediment transport and bed shear stress patterns in the Casamance estuary during high tide (22 February 2023 at 02:00) and low tide (21 February 2023 at 17:00). Bedload transport is generally low at high tide, with values near zero, except for a few upstream-directed peaks around 20 km. In contrast, low tide triggers a significant increase in bedload transport—especially between 0 and 30 km—marking it as a key phase for coarse sediment mobilisation.

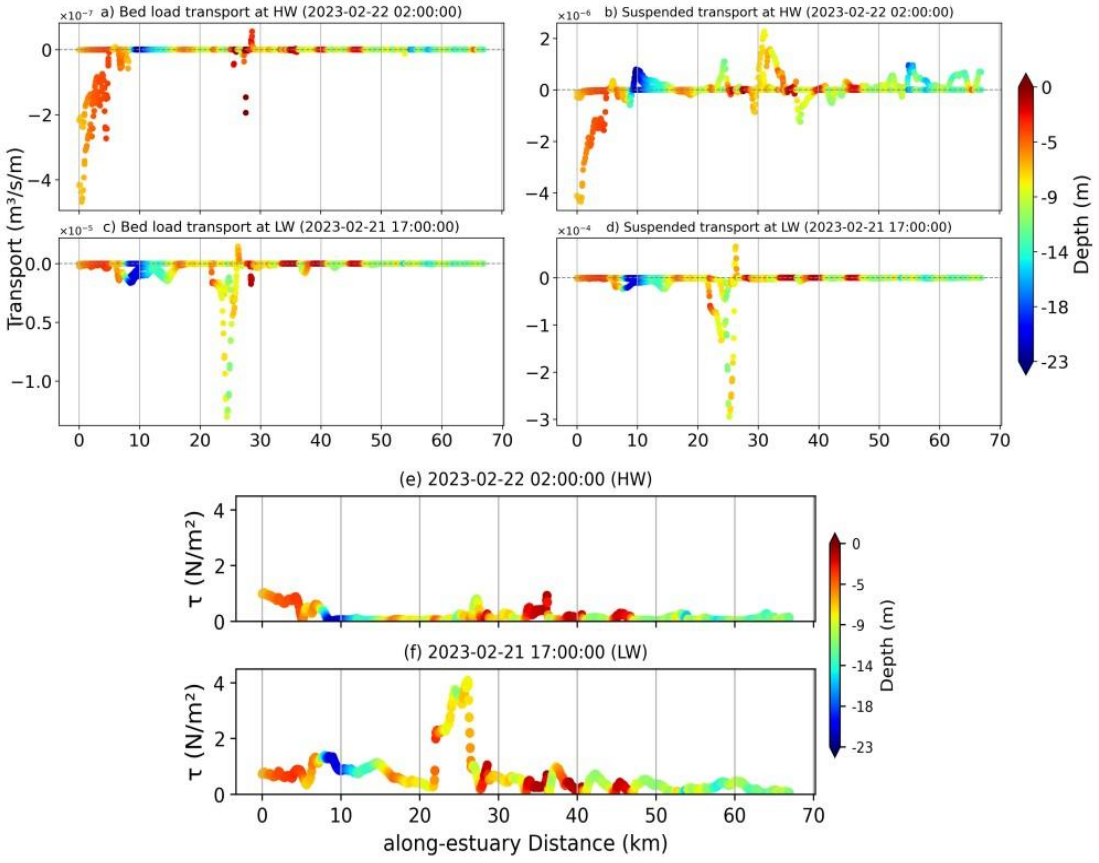

Figure 12. Longitudinal distribution of sediment transport (bedload and suspended load) and bed shear stress in the Casamance estuary during high tide (22 February 2023 at 02:00) and low tide (21 February 2023 at 17:00). The colours indicate bed depth (in metres), and the area between 20 and 45 km corresponds to the confluence with the Diouloulou and Thionck Essyl rivers.

 doi:10.20944/preprints202507.2525.v1

Suspended load transport also intensifies during low tide, reaching up to 3×10^{-4} m³/s/m, nearly ten times higher than during high tide. This indicates the dominant role of ebb currents in resuspending fine sediments, particularly in shallow high-velocity zones.

Between 20 and 45 km, near the Diouloulou and Thionck Essyl confluence, sediment activity is enhanced by lateral inflows exceeding 2000 m³/s. These inflows alter concentration gradients and shear stress distribution, contributing to localised sediment dynamics.

Bed shear stress reaches up to 4 N/m² during low tide (compared to <2 N/m² at high tide), with intense activity around 0–30 km and beyond 50 km—especially near tributary junctions.

This Figure 12 indicates the pivotal function of the low tide phase in the mobilisation of sediment within the Casamance estuary. Furthermore, it emphasises the significance of lateral inputs in shaping sediment dynamics, particularly within the confluence zone. This is a critical element that must be considered in any estuarine modelling or integrated management approach.

Overall, low tide emerges as the critical driver of sediment mobilisation, and the role of lateral inputs is essential for accurately modelling and managing sediment dynamics in the estuary.

The Figure13 illustrates the distribution of maximum bed shear stress (in N/m²) at the mouth of the Casamance estuary near Carabane Island during two tidal conditions. During spring tides, the shear stresses are significantly higher, reaching up to 4 N/m² during the flood tide (22 February 2023 at 22:00) and around 3 N/m² during the ebb tide (22 February 2023 at 04:00). The elevated values observed in the primary channels are indicative of intense hy-drodynamic activity, which is conducive to the resuspension of sediment. Conversely, during neap tide (1 March 2023), the stresses remained low, generally below 1.5 N/m² during both the flood (04:00) and the ebb (10:00), with a more diffuse distribution. The findings under-score a pronounced cyclical variability in bottom energy, exhibiting a conspicuously height-ened erosive potential during spring tides as compared to neap tides.

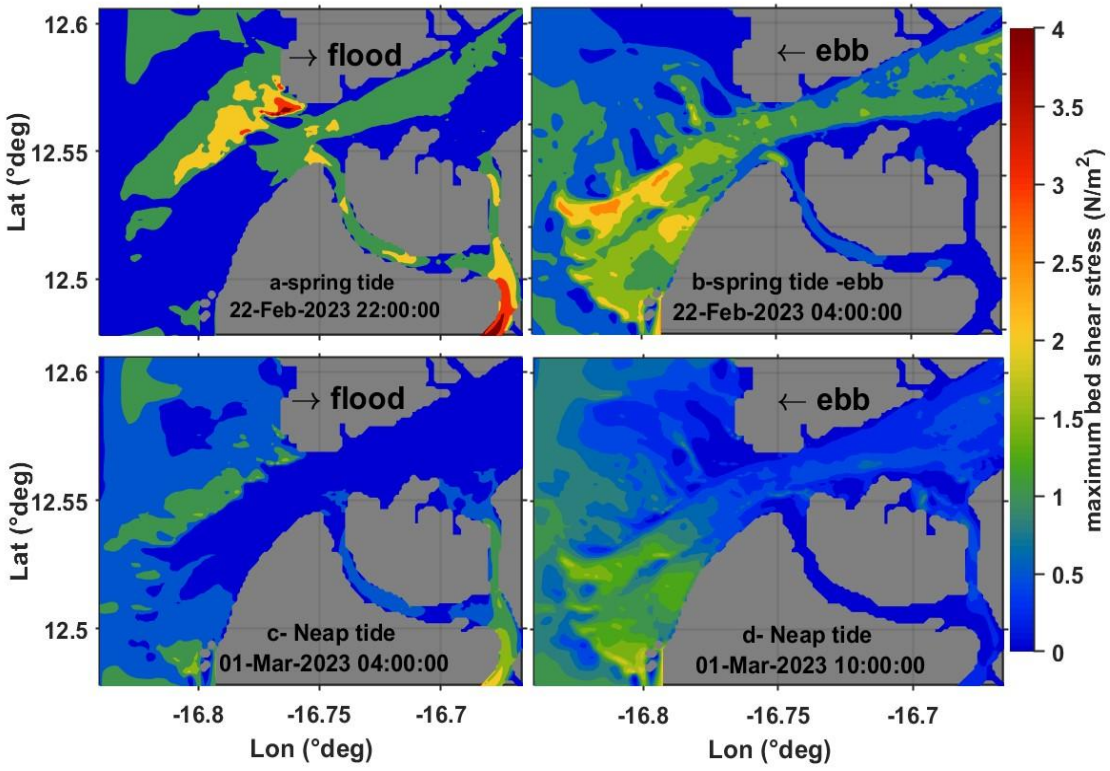

Figure 13. Maximum bed shear stress (in N/m²) at the mouth of the Casamance estuary near Carabane Island during spring and neap tide phase.

 doi:10.20944/preprints202507.2525.v1

Figure 14 illustrates total horizontal sediment transport in the Casamance estuary under spring and neap tides, highlighting strong contrasts between tidal phases. Under spring tide conditions, both flood and ebb phases show highly intense transport, especially in the northern main channel, with peak values exceeding 1.5×10^{-4} $m^3 \cdot s^{-1} \cdot m^{-1}$. This indicates vigorous bidirectional exchanges and substantial sediment mobilisation.

In contrast, neap tides display much weaker and more diffuse transport during both flood and ebb phases, due to the reduced tidal range and energy. These conditions suggest a tendency for sediment trapping within the estuary.

Overall, this configuration with MORFAC = 10 demonstrates how tidal regime strongly governs sediment dynamics, with spring tides promoting active redistribution and neap tides favouring temporary retention. However, the high transport intensities simulated under this setting may lead to exaggerated morphodynamic responses.

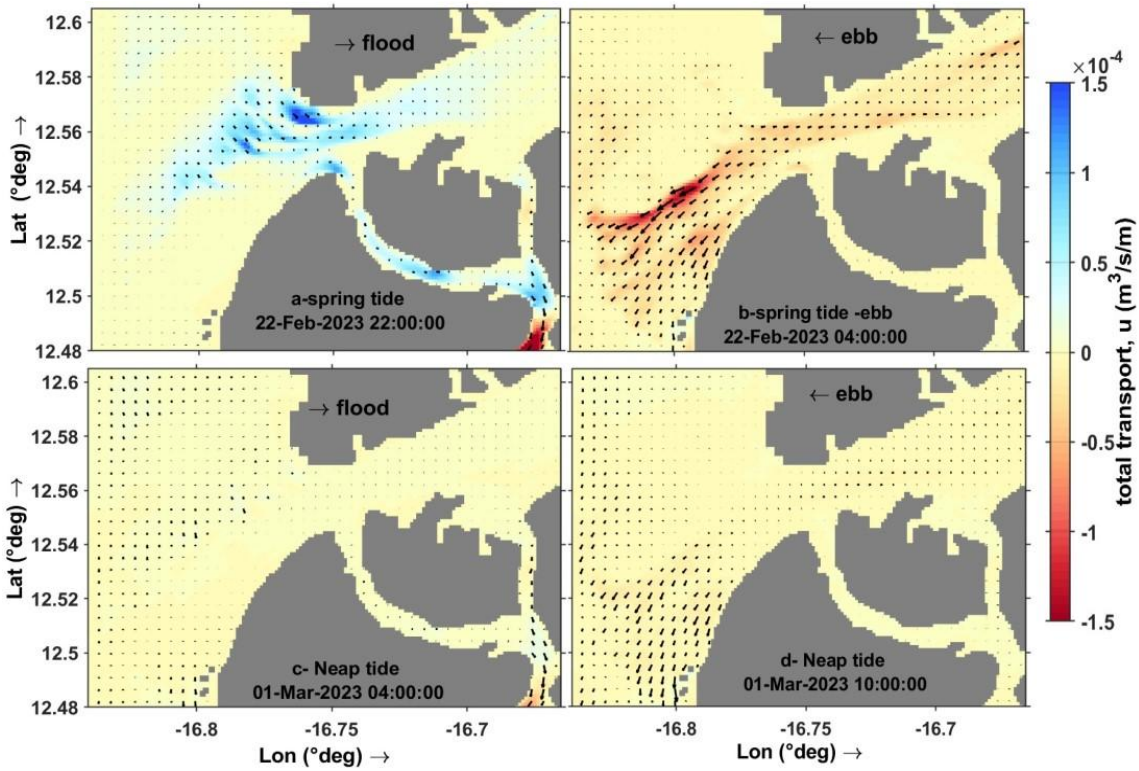

Figure 14. Use MORFAC=10, Total horizontal transport ($m^3 s^{-1} m^{-1}$) of sediment fractions (45 μm, 90 μm, 200 μm) at the mouth of the Casamance estuary near Carabane Island during spring and neap tide phase.

3.5.2. Situation MORFAC=01

The figure presents the total horizontal sediment transport (in $m^3/s/m$) at the mouth of the Casamance estuary, considering three representative grain-size classes (45 μm, 90 μm, and 200 μm). The execution of simulations with a MORFAC value of 1 during the spring tide (22 February 2023) and the neap tide (1 March 2023) has resulted in the revelation of substantial spatio-temporal variability.

During the spring tide flood (22 February at 10:00 UTC), the sediment flux reaches up to 3.5×10^{-5} $m^3/s/m$, particularly in the vicinity of Carabane Island. Transport is principally directed upstream, thereby feeding the channels, with partial diversion along the Nikine spit, which may potentially lead to deposition. The flow persists through the western channel between Nikine and Kafar towards Elinkine, where alternating zones of shoal deposition and localised erosion occur.

During the ebb (22 February at 04:00 UTC), intense westward export was observed in the Diogué area, indicating strong erosive activity. In such conditions, the Kafountine spit functions as an erodible barrier.

 doi:10.20944/preprints202507.2525.v1

Conversely, during the neap tide (1 March 2023), transport is weaker, with diffuse and low-magnitude fluxes, particularly in the vicinity of Carabane and Diogué.

The results demonstrate a clear and distinct pattern: Diogué functions as an active sediment outlet during the ebb of spring tides, while Carabane operates as a zone of transit or temporary trapping during flood. This behaviour is driven by local morphology, current regimes, and tidal dynamics.

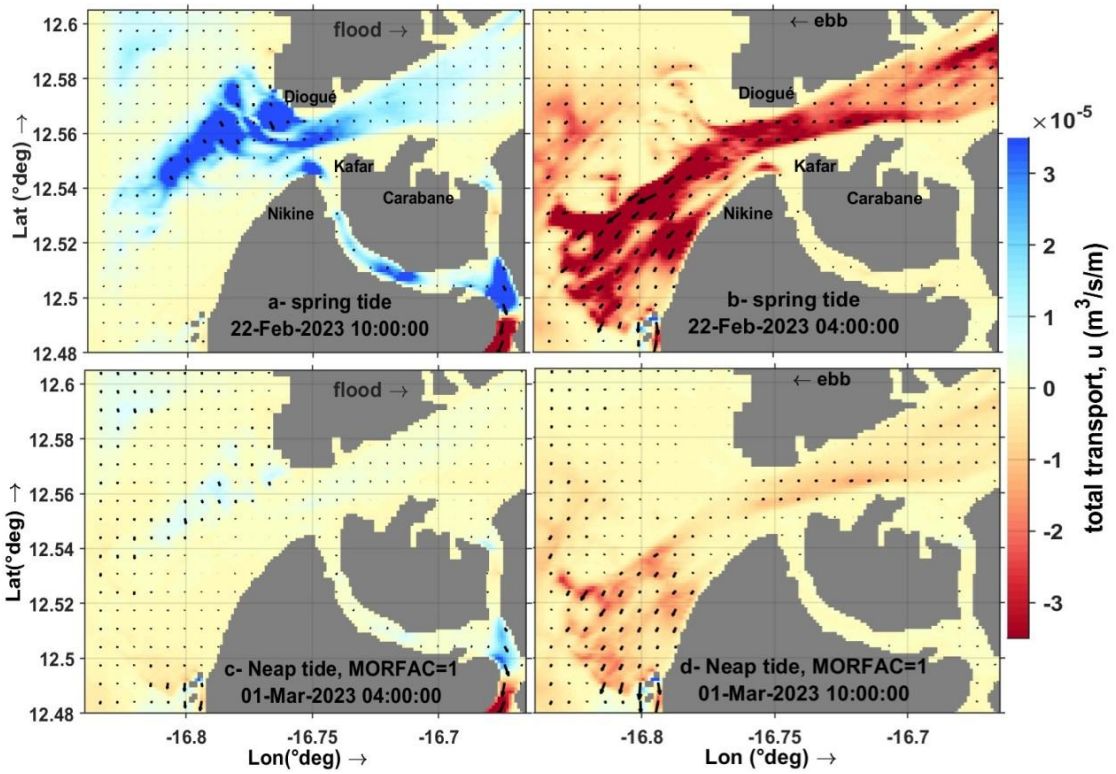

Figure 15. Use MORFAC=1, Total horizontal transport ($m^3s^{-1}m^{-1}$) of sediment fractions (45 μm, 90 μm, 200 μm) at the mouth of the Casamance estuary near Carabane Island during spring and neap tide phase.

4. Discussion: Interest and Limitations of SWOT Use

4.1. Model Performance

The analysis of the performance of the Delft3D and TPXO8 models to simulate the water levels of the Casamance estuary highlights notable differences in terms of accuracy and representation of hydrodynamic variations. The Delft3D model, calibrated with the in situ data, shows a better match with SWOT observations, with higher R^2 values and a significant reduction in RMSE and MAE errors. Conversely, TPXO8 underestimates water level variations in the upstream sections of the estuary, where the influence of continental inputs and interactions with complex bathymetry are more pronounced. This observation show the limitations of global models in tropical estuarine environments, as already suggested by several studies.

The spatial distribution of errors reveals a significant variability between the upstream and downstream parts of the estuary. The discrepancy between the simulations and the SWOT observations is particularly pronounced in the intermediate zone, which is influenced by turbulence and instability phenomena. This area, characterized by complex interactions between ocean forcings and tributaries, remains difficult to model, especially since the contribution of these tributaries to the dynamics of the system has not yet been well documented. In addition, SWOT performances to represent water level dynamics in Casamance have been validated in other environments, such as the Central Basin of the Congo Basin, where comparisons with altimetry data (Sentinel-3A/B, Jason-

 doi:10.20944/preprints202507.2525.v1

3, Sentinel-6A) and GEDI data show very high correlation coefficients of 0.977 (with a bias of 0.538 m) and 0.992 (with a bias of 1.011 m), respectively [40].

The consistency observed between the water levels from the SWOT mission and the data from the models, both on the right bank (Carabane station, Pc) and on the left bank (Diogué station, Pd), testifies to SWOT's ability to accurately represent water level variations in coastal areas with a high density of residential and port infrastructure. However, the relatively low temporal resolution of SWOT (21 days) is an important limitation. It does not capture short-period cyclical variations, especially those related to the tide, nor does it correctly reproduce the harmonic components of the tidal signal.

The use of SWOT data in this work is of major interest for improving the calibration of the Delft3D model, especially in poorly instrumented environments. These satellite observations, characterized by centimeter accuracy and wide spatial coverage, make it possible to refine the representation of simulated water levels, while contributing to the reduction of uncertainties associated with friction and viscosity parameters. In the case of the Casamance estuary, only upstream and downstream have tide gauge stations, leaving the intermediate zone and the tributaries in an observational shadow zone. This limitation considerably complicates the validation of hydrodynamic simulations. The contribution of SWOT data is therefore essential to fill these spatial gaps and strengthen the reliability of the model, in particular by providing observations on previously inaccessible sections of the estuarine system. Thus, SWOT is a particularly relevant calibration and validation tool in tropical and estuarine contexts with little equipment.

It is important to acknowledge the limitations of the approach adopted in this study. The SWOT product provides total water surface elevation without distinguishing between tidal, fluvial or atmospheric components. By contrast, the Delft3D model enables the use of various forcings, such as tides, river discharge and wave-induced processes. At this stage of the work, however, only tidal forcing was considered, based on the purely tidal TPXO8 model. Wave forcing was not included as the wave module was not activated.

Furthermore, sediment transport simulations were conducted from January to March, which corresponds to the dry season when river discharge in the Casamance estuary is very low. This hydrological context justifies the omission of fluvial forcing at this stage of the modelling process.

A new series of simulations is currently being developed to incorporate the combined effects of tides and river discharge during the rainy season (from June to October), as well as the influence of wave action.

4.2. Morphodynamic Sensitivity to the MORFAC Coefficient

The comparison of simulations with different morphological acceleration factors (MORFAC=1, 2, 5, 10, and 450) highlights a quasi-linear sensitivity of the model to this parameter (Figure 16). For MORFAC at 10, the rate of sediment transport is observed to be significantly enhanced, with an order of magnitude increase. This results in bathymetric changes that exceed in situ observations by up to 10 metres, with a mean bias of -0.056 metres and a mean absolute error (MAE) of 0.421 metres. At MORFAC at 450, this discrepancy reaches over 15 metres, and the MAE peaks at 2.459 metres. This confirms that such high acceleration factors generate unrealistic morphodynamic responses. Whilst the reduction of MORFAC to 5 and 2 does indeed result in a decrease of the transport intensity to 50% and 20% of that with MORFAC=10, the associated mean absolute errors (0.375 m and 0.307 m, respectively) and mean biases (+0.248 m and +0.261 m) continue to indicate significant overestimations of deposition (2–5 m in some areas), with the spatial distribution of erosion and accumulation remaining largely unchanged.

In contrast, MORFAC=1 yields the most realistic results, with a mean absolute error (MAE) of 0.286m and a mean bias of 0.266m, aligning closely with the surveyed bathymetry at key channel and shoal locations. Transport magnitudes ($2–3\times10^{-5} m^3 s^{-1} m^{-1}$) are consistent with field measurements, and overall morphodynamic trends remain within a ±1m margin of error. These findings demonstrate that while elevated MORFAC values have the capacity to expedite sediment dynamics, this occurs at

 doi:10.20944/preprints202507.2525.v1

the expense of physical realism. It is therefore concluded that MORFAC=1 offers the optimal compromise and should be favoured for reliable morphological simulations in the Casamance estuary.

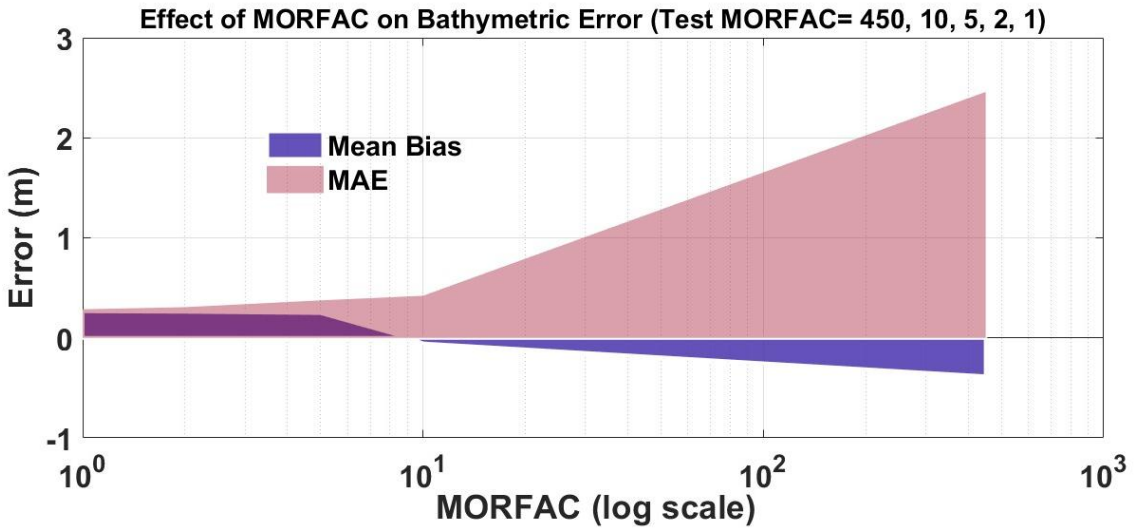

Figure 16. The following study will examine the relationship between the morphological acceleration factor (MORFAC) and model error metrics. The mean bias and mean absolute error (MAE) are plotted against MORFAC values on a logarithmic scale, thus emphasising the sensitivity of morphodynamic predictions to this parameter. MORFAC has been demonstrated to yield the lowest errors, whereas higher values have been shown to produce significant overestimations of bed level change.

4.3. Sediment Distribution Under the Influence of the Tide

Upstream of Ziguinchor, the sedimentary dynamics are weak, dominated by progressive settling due to the low energy of the currents (as shown in section 4.3). The majority of suspended particles are deposited in this area, contributing to the filling of lateral areas and tributaries. In the intermediate zone (between Pointe Saint-Georges and the Seleki Sector), sediments are suspended in the water column during the rising tide phases, but their transport is limited by the reduction in the energy of the currents as we go up the estuary. At Carabane and at the mouth, tide gauge hydrodynamics are more intense, leading to continuous suspension of fine sediments and more marked sediment transport to the ocean.

During spring water, the energy of the currents is sufficient to mobilize coarser sediments in the main channels (see section 4.3). This results in local erosion and redistribution of deposits to lower energy areas, including shorelines and sandbanks. In neap tides, sediment transport is reduced, favouring the accumulation of suspended sediments in areas of low turbulence (side arms, mangroves and bay bottoms). The spatial dynamics of the sediments impact the evolution of sandy banks and channels. The accumulation of sediments upstream can lead to progressive silting, while at the mouth, the morphology of the coastline is influenced by the transport of sediments to the ocean.

4.4. Implication of Hydraulic Slope on the Dynamic Hydro-Morpho Process

The analysis presented in Figure 17 compares the longitudinal free-surface slope (S_0, in m/km) derived from SWOT satellite observations with that simulated using the Delft3D model for the Casamance estuary. Panel (a) illustrates the correlation between both estimates. Positive slopes ($S_0 > 0$), corresponding to downstream flow during ebb tide, are shown in blue, while orange points reflect negative or near-zero slopes ($S_0 \leq 0$), often linked to rising tides or reversals in the hydraulic gradient. The linear regression shows a good agreement between the two datasets ($r = 0.71$), with a slope of 0.71 and an intercept of 0.002. However, the model tends to slightly underestimate positive slopes

 doi:10.20944/preprints202507.2525.v1

and overestimate the negative ones compared to SWOT data. The 1:1 line (y = x) serves as a visual benchmark for this deviation.

Panel (b) presents the error distribution $\Delta S_0 = S_{0(model)} - S_{0(SWOT)}$, which appears centred around zero and approximately bell-shaped. This indicates overall consistency between model outputs and observations, despite some dispersion. The root mean square error (RMSE) is 0.007 m/km and the mean absolute error (MAE) is 0.005 m/km. This level of accuracy is acceptable and highlights the capability of the Delft3D model to reproduce the estuarine slope dynamics observed by SWOT, although uncertainties remain due to the temporal/spatial resolution of SWOT and simplifications in the model.

These results shed light on the fundamental role of the hydraulic slope in shaping the estuarine hydro-morphodynamics. Firstly, the variation between flood and ebb slopes reflects a phase shift in water level dynamics, driven by tidal forces and modulated by friction and channel morphology (see Section 3.2). Steeper slopes during flood tides indicate strong tidal forcing from the ocean, whereas flatter slopes during ebb suggest a delayed response in estuarine drainage. This asymmetry contributes to observed trends in extreme water levels, particularly the rise in Low Water Spring (LWS) levels at Ziguinchor (Diouf et al., 2025), located upstream in the estuary.

Secondly, a steeper slope during the flood phase favours upstream transport of suspended sediments, enhancing morphological change in the riverbed. In contrast, the slower ebb reduces sediment evacuation and promotes temporary resuspension and deposition processes, as observed in Section 3.4. These variations directly influence sediment pathways and estuarine morphology over time.

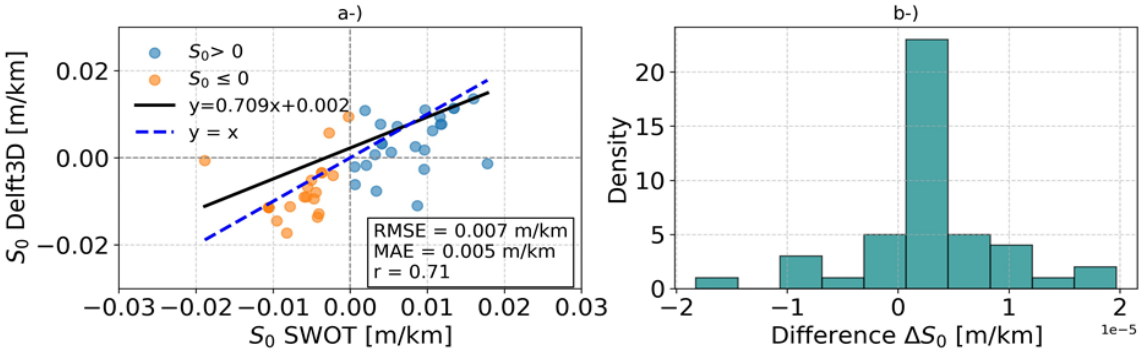

Figure 17. Comparison of the slope of the free surface (S0) between SWOT observations and Delft3D simulations in the Casamance estuary: (a) linear relationship between S0SWOT and S0Delft3 , (b) distribution of differences ΔS0.

5. Conclusions

The use of SWOT observations into the hydrodynamic modelling of estuaries is a major asset, allowing extended spatial coverage with centimeter accuracy. The system studied in this work presents a complex configuration, composed of a 70 km long main channel (from upstream to downstream), bordered by tributaries and bolongs that ensure the exchange of water masses between rivers, rice fields, mangroves and the ocean.

SWOT data provided valuable information on water levels and flows throughout the domain, particularly in the intermediate zone (Pointe Saint-Georges sector) and in tributaries for which no reference tide gauge data was available to our knowledge. These observations also validated and adjusted the interpolated bathymetry of the main channel and tributaries. Overall, this bathymetry correctly reproduces the dynamics of the tide over the entire area.

However, significant phase shifts and errors were observed on the tributary of the Tendouck sector, probably related to a limited quality of the bathymetric data, which were not calibrated with in situ measurements. This area therefore remains to be improved to refine the results of the model.

 doi:10.20944/preprints202507.2525.v1

The three-dimensional hydromorphodynamic model faithfully reproduces the tide as well as the horizontal and vertical circulation within the estuary, which is confirmed by data from sensors installed upstream and downstream. The water levels simulated by Delft3D show good agreement with SWOT observations, especially in the main channel, especially in the open area towards the sea at the mouth of the Casamance, as well as at the upstream border of the estuary.

However, significant differences persist in the intermediate zone, which is particularly dynamic, under the influence of the tributaries of Diouloulou and Tionk Essyl. These discrepancies highlight the need for refinement of the model, in particular by improving bathymetric data and integrating additional observations in the Pointe Saint-Georges sector, as well as on all the bolongs and tributaries of the Casamance. This would make it possible to move towards an integrated multi-sensor modelling, more representative of the complex hydrodynamic exchanges in this area.

Author Contributions: Conceptualization, A.D., E.S., J.D., R.L., I.S.; methodology, A.D., E.S., J.D., R.L.; software, A.D., E.S., and C.L.; validation, E.S., J.D., I.S., B.S., I.T., R.L., Y.Y., and Z.Z.; formal analysis, A.D., E.S., J.D.; investigation, A.D.,E.S.,B.S.,I.S. and J.D; resources, J.D., E.S., and I.S.; data curation, A.D., E.S., and J.D.; writing—original draft preparation, A.D.; writing—review and editing, E.S., I.T.; visualization, A.D.; supervision, E.S., J.D., R.L., I.S., B.S., I.T.; project administration, J.D.; funding acquisition, J.D., I.S., E.S All authors have read and agreed to the published version of the manuscript.

Funding: This research did not receive external funding apart from institutional support. Fieldwork missions were supported by the Directorate of Environment and Classified Establishments (DEEC) of the Ministry of Environment and Sustainable Development, Senegal, and by the LOSEC research team. A research stay was funded through a SCAC internship grant provided by the French Embassy in Dakar.

Data Availability Statement: The SWOT Level-2 high-resolution pixel cloud product (L2_HR_PIXC), used in this study, is publicly available and can be accessed via https://hydroweb.next.theia-land.fr/ and https://search.earthdata.nasa.gov/. Additional datasets generated or analysed during the current study, including Delft3D model outputs and in situ water level observations from the Casamance estuary, are available from the corresponding author on reasonable request.

Acknowledgments: The authors would like to express their gratitude to the Directorate of Environment and Classified Establishments (DEEC) of the Ministry of Environment and Sustainable Development (MEDD), Senegal, for funding the field campaigns, and to the French Embassy in Dakar for the SCAC internship grant, which provided the financial support necessary to undertake this research at the M2C — Continental and Coastal Morphodynamics — UMR 6143. The authors also sincerely thank the M2C laboratory for its scientific hospitality during research stays, the provision of high-performance computing resources used for Delft3D simulations, and access to SWOT satellite data. Appreciation is extended to the Department of Geology at the Faculty of Sciences and Techniques of Cheikh Anta Diop University (UCAD), Senegal, for its academic support, as well as to all the researchers from the LOSEC team who actively participated in the data collection missions in the Casamance region.

Conflicts of Interest: The authors declare no competing interests.

Abbreviations

The following abbreviations are used in this manuscript:

AWAC ADCP	Acoustic Doppler Current Profiler
HFD	Height–Fall–Discharge
HW	High Water
LW	Low Water
LWS	Low Water Spring
MAE	Mean Absolute Error
MORFAC	Morphological Acceleration Factor
MHWS	Mean High Water Springs
MLWS	Mean Low Water Springs

 doi:10.20944/preprints202507.2525.v1

RMSE	Root Mean Square Error
WSE	Water Surface Elevation
SWOT	Surface Water and Ocean Topography

Appendix A

Appendix A.1

Table A1. Summary of the main characteristics of the collected data.

Instrument	Location	Depth (m)	Acquisition Period	Resolution (min)	Data
Aquadopp	ST3: Ziguinchor pontoon, 70 km upstream	3	20 jan-22 jul 2023	10	Current velocity and water level
	ST1: Carabane pontoon downstream	8	21 jan - 23 Apr 2023	10	
AWAC ADCP	ST0: 5 km from the mouth	6	11 Nov-02 Dec 2012	15	Current velocity (30 cells of 50 cm) and water level
AWAC ADCP	ST4: Mid-channel a Ziguinchor	9	21 Nov -22 Nov 2021	1	Current velocity (cells of 50 cm) and water level
	ST2: Mid-channel Carabane	14	23 Nov -24 Nov 2021	1	

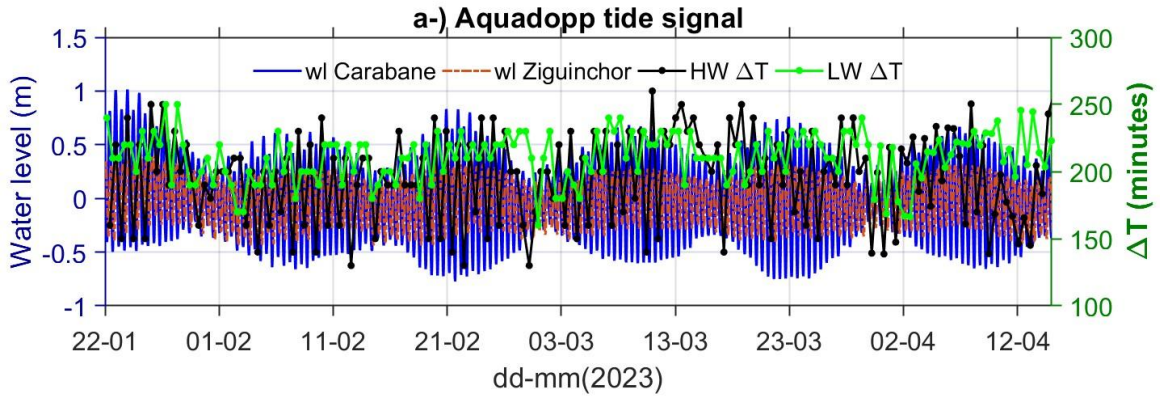

Figure A1. The temporal discrepancy in the propagation of tidal waves between Carabane (estuary mouth) and Ziguinchor (upstream) has been determined through analysis of Aquadopp tide gauge recordings. The levels of water at both stations are displayed, in addition to the time delay (ΔT, in minutes) between high tides (HW) and low tides (LW). This figure A1 illustrates the time lag of the tidal wave between Carabane and Ziguinchor over the period from January to April 2023. The data were recorded at 30-second intervals by Aquadopp sensors and subsequently averaged over 10-minute intervals for the purpose of analysis. The water level signal at Carabane (blue curve) precedes that at Ziguinchor (red dashed curve), indicating upstream propagation of the tidal wave. The time lag between high tides (black dots) and low tides (green dots) varies primarily between 150 and 250 minutes, reflecting the progressive distortion and attenuation of the tidal wave along the estuary. **MHWS (Mean High Water Springs) and MLWS (Mean Low Water Springs).**

 doi:10.20944/preprints202507.2525.v1

Appendix B

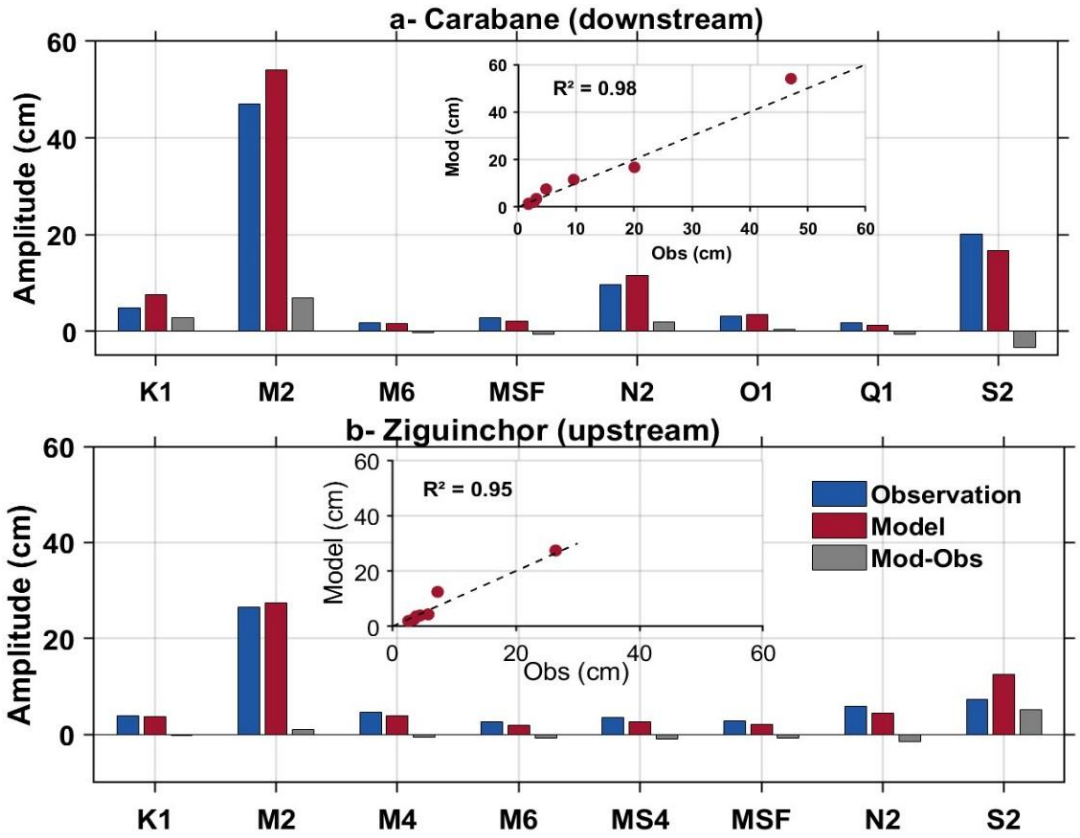

Figure A2. Comparison of observed and simulated tidal harmonic amplitudes (Delft3D model) at the Carabane (a) and Ziguinchor (b) stations. Grey bars represent the differences between observations and model outputs. The inset shows the linear correlation (R^2) between observed and modelled amplitudes. The Delft3D model reproduces the main tidal constituents well, particularly M2, with good agreement at both Carabane and Ziguinchor. However, discrepancies are noted for S2 (underestimated downstream, overestimated upstream), and diurnal constituents such as K1 and O1 are consistently underestimated. Non-linear constituents (M4, M6, MSF) are slightly overestimated, especially upstream. Despite these differences, the overall correlation remains high (R^2 = 0.98 at Carabane and 0.95 at Ziguinchor), indicating that dominant tidal dynamics are well represented.

 doi:10.20944/preprints202507.2525.v1

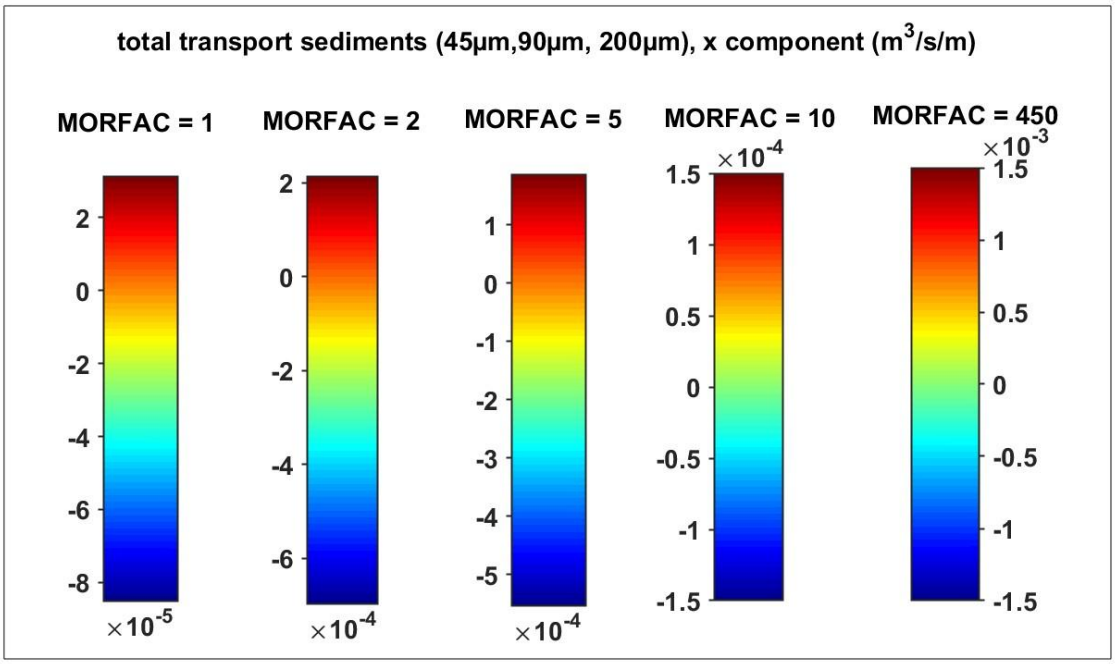

Figure A3. The present study investigates the influence of the MORFAC coefficient on total longitudinal sediment transport (x-component, in $m^3/s/m$), based on simulations with five increasing values of MORFAC (1, 2, 5, 10, 450) and three sediment size fractions (45, 90, and 200 µm). In the context of morphodynamic modelling at the mouth of the Casamance estuary, the MORFAC (Morphological Acceleration Factor) plays a critical role in balancing physical realism and computational efficiency. A sensitivity analysis was conducted by testing five MORFAC values (1, 2, 5, 10, 450). The results demonstrate a progressive increase in sediment transport intensity with increasing MORFAC, particularly beyond MORFAC = 10, where transport rates become unrealistically high. This underscores the necessity for meticulous calibration to circumvent numerical artefacts and to guarantee reliable morphological inferences.

References

1. J. Albergel, "Une méthode 'expert' pour la conception des barrages anti-sel dans les bas-fonds de Basse et Moyenne Casamance," *Conservation et utilisation durable des ressources naturelles du bassin hydrographique de la Casamance, Annales du séminaire tenu du 22 au 26 octobre 1990 à Ziguinchor (Sénégal))*, no. October, pp. 75–82, 1992.
2. H. Dacosta, "Precipitations et ecoulements sur le bassin de la Casamance," *Th. Doctorat*, p. 277, 1989.
3. J.-C. Olivry, "Les conséquences durables de la sécheresse actuelle sur l'écoulement du fleuve Sénégal et l'hypersalinisation de la basse Casamance," *The Influence of Climate Change and Climatic Variability on the Hydrologie Regime and Water Resources*, vol. 3, no. May, pp. 501–512, 1987.
4. J. P. Montoroi and J. Albergel, "L'intervention des hydrologues et pédologues de l'ORSTOM en Casamance," *Conservation et utilisation durable des ressources naturelles du bassin hydrographique de la Casamance*, no. October 2015, pp. 96–99, 1993.
5. M. Bacci, M. Diop, and M. Pasqui, "Rapport n°6 Décembre 2013 CLIMAT Encadrement climatique et évaluation du changement climatique dans les régions d'étude."
6. P. M. Sadio, M. L. Mbaye, S. Diatta, and M. B. Sylla, "Hydro-climate variability and change in the Casamance river basin (Senegal)," *Houille Blanche*, vol. 2021-March, no. 6, pp. 89–96, 2020, doi: 10.1051/lhb/2021002.
7. W. Han, C. Huang, J. Gu, J. Hou, Y. Zhang, and W. Wang, "Water Level Change of Qinghai Lake from ICESat and ICESat-2 Laser Altimetry," *Remote Sens (Basel)*, vol. 14, no. 24, Dec. 2022, doi: 10.3390/rs14246212.

 doi:10.20944/preprints202507.2525.v1

8. K. Xu, C. Wang, and L. Bin, "Compound flood models in coastal areas: a review of methods and uncertainty analysis," *Natural Hazards*, pp. 1–28, 2022.
9. L. Yu, H. Zhang, W. Gong, and X. Ma, "Validation of Mainland Water Level Elevation Products From SWOT Satellite," *IEEE J Sel Top Appl Earth Obs Remote Sens*, vol. 17, pp. 13494–13505, 2024, doi: 10.1109/JSTARS.2024.3435363.
10. H. Wang, Y. Chu, Z. Huang, C. Hwang, and N. Chao, "Robust, long-term lake level change from multiple satellite altimeters in Tibet: Observing the rapid rise of Ngangzi Co over a new wetland," *Remote Sens (Basel)*, vol. 11, no. 5, Mar. 2019, doi: 10.3390/rs11050558.
11. H. Oubanas, I. Gejadze, P. O. Malaterre, and F. Mercier, "River discharge estimation from synthetic SWOT-type observations using variational data assimilation and the full Saint-Venant hydraulic model," *J Hydrol (Amst)*, vol. 559, no. 2018, pp. 638–647, 2018, doi: 10.1016/j.jhydrol.2018.02.004.
12. G. Ramillien, F. Frappart, and L. Seoane, "Application of the regional water mass variations from GRACE satellite gravimetry to large-scale water management in Africa," *Remote Sens (Basel)*, vol. 6, no. 8, pp. 7379–7405, 2014, doi: 10.3390/rs6087379.
13. A. Taveneau et al., "Observing and predicting coastal erosion at the langue de barbarie sand spit around saint louis (Senegal, west africa) through satellite-derived digital elevation model and shoreline," *Remote Sens (Basel)*, vol. 13, no. 13, Jul. 2021, doi: 10.3390/rs13132454.
14. D. B. Angnuureng et al., "Satellite, drone and video camera multi-platform monitoring of coastal erosion at an engineered pocket beach: A showcase for coastal management at Elmina Bay, Ghana (West Africa)," *Reg Stud Mar Sci*, vol. 53, p. 102437, 2022, doi: 10.1016/j.rsma.2022.102437.
15. E. T. Mendoza et al., "Coastal flood vulnerability assessment, a satellite remote sensing and modeling approach," *Remote Sens Appl*, vol. 29, no. December 2022, p. 100923, 2023, doi: 10.1016/j.rsase.2023.100923.
16. R. Almar, E. W. J. Bergsma, P. Maisongrande, and L. P. M. de Almeida, "Wave-derived coastal bathymetry from satellite video imagery: A showcase with Pleiades persistent mode," *Remote Sens Environ*, vol. 231, p. 111263, Sep. 2019, doi: 10.1016/J.RSE.2019.111263.
17. E. W. J. Bergsma, R. Almar, E. J. Anthony, T. Garlan, and E. Kestenare, "Wave variability along the world's continental shelves and coasts: Monitoring opportunities from satellite Earth observation," *Advances in Space Research*, vol. 69, no. 9, pp. 3236–3244, 2022, doi: 10.1016/j.asr.2022.02.047.
18. R. Almar et al., "Response of the Bight of Benin (Gulf of Guinea, West Africa) coastline to anthropogenic and natural forcing, Part1: Wave climate variability and impacts on the longshore sediment transport," *Cont Shelf Res*, vol. 110, pp. 48–59, Nov. 2015, doi: 10.1016/j.csr.2015.09.020.
19. E. J. Anthony et al., "Response of the Bight of Benin (Gulf of Guinea, West Africa) coastline to anthropogenic and natural forcing, Part 2: Sources and patterns of sediment supply, sediment cells, and recent shoreline change," *Cont Shelf Res*, vol. 173, pp. 93–103, Feb. 2019, doi: 10.1016/J.CSR.2018.12.006.
20. A. Diouf et al., "Urban beach evolution in Saint Louis, Senegal (West Africa) using shore-based camera video monitoring as a management tool," *Reg Stud Mar Sci*, vol. 83, Apr. 2025, doi: 10.1016/j.rsma.2025.104050.
21. A. N. Klotz et al., "Nearshore satellite-derived bathymetry from a single-pass satellite video: Improvements from adaptive correlation window size and modulation transfer function," *Remote Sens Environ*, vol. 315, no. March, p. 114411, 2024, doi: 10.1016/j.rse.2024.114411.
22. P. Marchesiello et al., "Exploring Fine-Scale Satellite-Derived Coastal Bathymetry for Ocean Modeling: A Case Study from West Africa," *Estuaries and Coasts*, 2024, doi: 10.1007/s12237-024-01398-9.
23. K. Pajak, M. Idzikowska, and K. Kowalczyk, "Relationship of Satellite Altimetry Data, and Bathymetry Observations on the West Coast of Africa," *J Mar Sci Eng*, vol. 11, no. 1, 2023, doi: 10.3390/jmse11010149.
24. D. B. Angnuureng et al., "Video oberservation of waves and shoreline change on the microtidal james town beach in Ghana," in *Journal of Coastal Research*, Coastal Education Research Foundation Inc., Mar. 2016, pp. 1022–1026. doi: 10.2112/SI75-205.1.
25. R. Almar et al., "Coastal Zone Changes in West Africa: Challenges and Opportunities for Satellite Earth Observations," *Surv Geophys*, vol. 44, no. 1, pp. 249–275, 2023, doi: 10.1007/s10712-022-09721-4.

 doi:10.20944/preprints202507.2525.v1

26. G. Abessolo Ondoa et al., "Sea level at the coast from video-sensed waves: Comparison to tidal gauges and satellite altimetry," *J Atmos Ocean Technol*, vol. 36, no. 8, pp. 1591–1603, 2019, doi: 10.1175/JTECH-D-18-0203.1.
27. A. Dièye, B. A. Sow, H. B. Dieng, P. Marchesiello, and L. Descroix, "Impact of climate variability modes on trend and interannual variability of sea level near the West African coast," *West African coast. African Journal of Environmental Science and Technology*, vol. 2023, no. 7, doi: 10.5897/AJEST2022.3173ï.
28. C. O. T. Cisse, E. K. Brempong, A. Taveneau, R. Almar, B. A. Sy, and D. B. Angnuureng, "Extreme coastal water levels with potential flooding risk at the low-lying Saint Louis historic city, Senegal (West Africa)," *Front Mar Sci*, vol. 9, no. December, 2022, doi: 10.3389/fmars.2022.993644.
29. C. Duncan, H. J. F. Owen, J. R. Thompson, H. J. Koldewey, J. H. Primavera, and N. Pettorelli, "Satellite remote sensing to monitor mangrove forest resilience and resistance to sea level rise," *Methods Ecol Evol*, vol. 9, no. 8, pp. 1837–1852, 2018, doi: 10.1111/2041-210X.12923.
30. C. M. Birkett, L. A. K. Mertes, T. Dunne, M. H. Costa, and M. J. Jasinski, "Surface water dynamics in the Amazon Basin: Application of satellite radar altimetry," *Journal of Geophysical Research: Atmospheres*, vol. 107, no. 20, p. LBA 26-1-LBA 26-21, 2002, doi: 10.1029/2001JD000609.
31. F. Frappart, S. Calmant, M. Cauhopé, F. Seyler, and A. Cazenave, "Preliminary results of ENVISAT RA-2-derived water levels validation over the Amazon basin," *Remote Sens Environ*, vol. 100, no. 2, pp. 252–264, Jan. 2006, doi: 10.1016/j.rse.2005.10.027.
32. A. T. Diepkilé, F. Egon, F. Blarel, E. Mougin, and F. Frappart, "Validation of the altimetry-based water levels from Sentinel-3A and B in the Inner Niger Delta," in *Proceedings of the International Association of Hydrological Sciences*, Copernicus GmbH, Nov. 2021, pp. 31–35. doi: 10.5194/piahs-384-31-2021.
33. S. Bogning et al., "Monitoring water levels and discharges using radar altimetry in an ungauged river basin: The case of the Ogooué," *Remote Sens (Basel)*, vol. 10, no. 2, Feb. 2018, doi: 10.3390/rs10020350.
34. S. Bogning et al., "Monitoring water levels and discharges using radar altimetry in an ungauged river basin: The case of the Ogooué," *Remote Sens (Basel)*, vol. 10, no. 2, Feb. 2018, doi: 10.3390/rs10020350.
35. F. Papa et al., "Satellite-derived surface and sub-surface water storage in the Ganges-Brahmaputra River Basin," *J Hydrol Reg Stud*, vol. 4, pp. 15–35, Sep. 2015, doi: 10.1016/j.ejrh.2015.03.004.
36. Y. Zhao, J. Fu, Z. Pang, W. Jiang, P. Zhang, and Z. Qi, "Validation of Inland Water Surface Elevation from SWOT Satellite Products: A Case Study in the Middle and Lower Reaches of the Yangtze River," *Remote Sens (Basel)*, vol. 17, no. 8, Apr. 2025, doi: 10.3390/rs17081330.
37. M. J. Tourian, O. Elmi, A. Mohammadnejad, and N. Sneeuw, "Estimating river depth from SWOT-type observables obtained by satellite altimetry and imagery," *Water (Switzerland)*, vol. 9, no. 10, pp. 1–22, 2017, doi: 10.3390/w9100753.
38. S. Wongchuig-Correa, R. Cauduro Dias de Paiva, S. Biancamaria, and W. Collischonn, "Assimilation of future SWOT-based river elevations, surface extent observations and discharge estimations into uncertain global hydrological models," *J Hydrol (Amst)*, vol. 590, no. August, p. 125473, 2020, doi: 10.1016/j.jhydrol.2020.125473.
39. E. H. Altenau, T. M. Pavelsky, M. T. Durand, X. Yang, R. P. de M. Frasson, and L. Bendezu, "The Surface Water and Ocean Topography (SWOT) Mission River Database (SWORD): A Global River Network for Satellite Data Products," *Water Resour Res*, vol. 57, no. 7, pp. 1–15, 2021, doi: 10.1029/2021WR030054.
40. C. Normandin et al., "First results of the surface water ocean topography (SWOT) observations to rivers elevation profiles in the Cuvette Centrale of the Congo Basin," *Frontiers in Remote Sensing*, vol. 5, no. October, pp. 1–16, 2024, doi: 10.3389/frsen.2024.1466695.
41. J. Bergeron, G. Siles, R. Leconte, M. Trudel, D. Desroches, and D. L. Peters, "Assessing the capabilities of the Surface Water and Ocean Topography (SWOT) mission for large lake water surface elevation monitoring under different wind conditions," *Hydrol Earth Syst Sci*, vol. 24, no. 12, pp. 5985–6000, 2020, doi: 10.5194/hess-24-5985-2020.
42. S. Wongchuig-Correa, R. Cauduro Dias de Paiva, S. Biancamaria, and W. Collischonn, "Assimilation of future SWOT-based river elevations, surface extent observations and discharge estimations into uncertain global hydrological models," *J Hydrol (Amst)*, vol. 590, Nov. 2020, doi: 10.1016/j.jhydrol.2020.125473.

 doi:10.20944/preprints202507.2525.v1

43. F. Rodrigues do Amaral, T. Pellarin, T. N. Trung, T. Anh Tu, and N. Gratiot, "Enhancing discharge estimation from SWOT satellite data in a tropical tidal river environment," *PLOS Water*, vol. 3, no. 2, p. e0000226, Feb. 2024, doi: 10.1371/journal.pwat.0000226.
44. Q. Bonassies et al., "Assimilation of SWOT Altimetry Data for Riverine Flood Reanalysis: From Synthetic to Real Data," Apr. 2025, [Online]. Available: http://arxiv.org/abs/2504.21670
45. A. B. V. Bôas, G. Marechal, and A. Bohé, "Observing Interactions Between Waves, Winds, and Currents from SWOT," Dec. 30, 2024. doi: 10.22541/essoar.173557501.11384934/v1.
46. M. Archer, J. Wang, P. Klein, G. Dibarboure, and L. L. Fu, "Wide-swath satellite altimetry unveils global submesoscale ocean dynamics," *Nature*, vol. 640, no. 8059, pp. 691–696, Apr. 2025, doi: 10.1038/s41586-025-08722-8.
47. Y. Brunet-Moret, "Etude des marées dans le fleuve Casmance," *Cahiers Orstom série Hydrologie*, vol. 7, no. 4, pp. 3–18, 1970.
48. A. Lahoud, "Modélisation des circulations transitoire et résiduelle: application à l'estuaire de la Casamance (Sénégal)," Academie de Montpellier, Universite des Sciences et Techniques du Languedocc, 1989.
49. A. Diouf et al., "The Influence of Tidal Distortion on Extreme Water Levels in Casamance Estuary, Senegal," *Estuaries and Coasts*, vol. 48, no. 2, Mar. 2025, doi: 10.1007/s12237-024-01459-z.
50. B. Ndom, S. Ndoye, B. A. Sow, and V. Echevin, "Tides in the Casamance estuary: A modeling study," *Cont Shelf Res*, vol. 285, Feb. 2025, doi: 10.1016/j.csr.2024.105389.
51. P. S. Diouf, J. Pagès, and J. L. Saos, "Géographie de l'estuaire de la Casamance," *L'estuaire de la Casamance: environnement, pêche, socioéconomie. Dakar: ISRA/CRODT*, pp. 13–22, 1986
52. Y. Badji, O. Diankha, and B. A. Sow, "Study of heavy metal contamination of Sarotherodon melanotheron and Crassostrea gasar in Casamance river (Senegal)," *Int. J. Biol. Chem. Sci*, vol. 19, no. 1, pp. 48–57, 2025, doi: 10.4314/ijbcs.v19i1.4.
53. A. Ndiaye, T. Mbaye, D. Ngom, M. O. Ly, and D. Diouf, "Fonctionnement Hydrique du Baobab (Adansonia digitata L.) en Moyenne et Haute Casamance (Sénégal)," *European Scientific Journal ESJ*, vol. 15, no. 3, Jan. 2019, doi: 10.19044/esj.2019.v15n3p292.
54. C. Faye, "ANALYSE DES TENDANCES DE LA DISTRIBUTION RÉGIONALE ET DE L'INTENSITÉ DES PRECIPITATIONS : UTILISATION D'INDICES CLIMATIQUES DANS LE BASSIN DE LA CASAMANCE (SENEGAL) ANALYSIS OF TRENDS IN REGIONAL DISTRIBUTION AND PRECIPITATION INTENSITY: THE USE OF CLIMATE INDICES IN THE CASAMANCE BASIN (SENEGAL)," 2018.
55. E. H. S. Diop$ and J. L. Saos$, "Evidence of dynamics reversal in tropical estuaries, geomorphological and sedimentological consequences (Salum and Casamance Rivers, Senegal)," 1985.
56. "1989 saos et al. Introduction_a_letude_sedimentologique_et_bathyme".
57. G. D. Egbert and S. Y. Erofeeva, "Efficient inverse modeling of barotropic ocean tides," *J Atmos Ocean Technol*, vol. 19, no. 2, pp. 183–204, 2002, doi: 10.1175/1520-0426(2002)019<0183:EIMOBO>2.0.CO;2.
58. G. D. Egbert, R. D. Ray, and B. G. Bills, "Numerical modeling of the global semidiurnal tide in the present day and in the last glacial maximum," *J Geophys Res Oceans*, vol. 109, no. 3, Mar. 2004, doi: 10.1029/2003jc001973.
59. D. Stammer et al., "Accuracy assessment of global barotropic ocean tide models," Sep. 01, 2014. doi: 10.1002/2014RG000450.
60. B. Kresning, M. R. Hashemi, S. P. Neill, J. A. M. Green, and H. Xue, "The impacts of tidal energy development and sea-level rise in the Gulf of Maine," *Energy*, vol. 187, p. 115942, 2019, doi: 10.1016/j.energy.2019.115942.
61. H. Fu et al., "Global ocean reanalysis CORA2 and its inter comparison with a set of other reanalysis products," *Front Mar Sci*, vol. 10, 2023, doi: 10.3389/fmars.2023.1084186.
62. Y. Cao et al., "Impact of trends in river discharge and ocean tides on water level dynamics in the Pearl River Delta," *Coastal Engineering*, vol. 157, Apr. 2020, doi: 10.1016/j.coastaleng.2020.103634.
63. X. Yu, W. Zhang, and A. J. F. Hoitink, "Impact of river discharge seasonality change on tidal duration asymmetry in the Yangtze River Estuary," *Sci Rep*, vol. 10, no. 1, pp. 1–17, 2020, doi: 10.1038/s41598-020-62432-x.
64. Deltares Systems, "3D/2D modelling suite for integral water solutions, DELFT3D-WAVE," pp. 1–110, 2020.

 doi:10.20944/preprints202507.2525.v1

65. L. Boudet, "Modélisation du transport sédimentaire lié aux tempêtes et aux crues à l'embouchure du Rhône," p. 224 pp., 2017.
66. E. P. L. Elias, D. J. R. Walstra, J. A. Roelvink, M. J. F. Stive, and M. D. Klein, "Hydrodynamic validation of Delft3D with field measurements at Egmond," in *Coastal engineering 2000*, 2001, pp. 2714–2727.
67. G. R. Lesser, J. A. v Roelvink, J. A. T. M. van Kester, and G. S. Stelling, "Development and validation of a three-dimensional morphological model," *Coastal engineering*, vol. 51, no. 8–9, pp. 883–915, 2004.
68. A. Luijendijk, "Validation, calibration and evaluation of a Delft3D-FLOW model with ferry measurements," *Civil Engineering*, vol. M.Sc., no. September, p. 92, 2001.
69. A. Mohammadian and T. R. Ghobrial, "26 IAHR International Symposium on Ice Two-dimensional numerical modelling of ice-jam flood in the Chaudière River using Delft3D-FLOW-Ice," no. June, 2022.
70. B. G. Ruessink, G. Ramaekers, and L. C. Van Rijn, "On the parameterization of the free-stream non-linear wave orbital motion in nearshore morphodynamic models," *Coastal Engineering*, vol. 65, pp. 56–63, 2012, doi: 10.1016/j.coastaleng.2012.03.006.
71. B. G. Ruessink, G. Ramaekers, and L. C. Van Rijn, "On the parameterization of the free-stream non-linear wave orbital motion in nearshore morphodynamic models," *Coastal Engineering*, vol. 65, pp. 56–63, 2012, doi: 10.1016/j.coastaleng.2012.03.006.
72. Z. B. Wang, M. C. J. L. Jeuken, H. Gerritsen, H. J. De Vriend, and B. A. Kornman, "Morphology and asymmetry of the vertical tide in the Westerschelde estuary," *Cont Shelf Res*, vol. 22, no. 17, pp. 2599–2609, 2002, doi: 10.1016/S0278-4343(02)00134-6.
73. Deltares, "3D/2D Modelling Suite for Integral Water Solutions, DELFT3D-FLOW," *Boussinesqweg 1 2629 HV Delft P.O. 177 2600 MH Delft The Netherlands*, pp. 1–110, 2024.
74. G. S. Stelling and J. A. T. M. Van Kester, "On the approximation of horizontal gradients in sigma co-ordinates for bathymetry with steep bottom slopes," *Int J Numer Methods Fluids*, vol. 18, no. 10, pp. 915–935, 1994, doi: 10.1002/fld.1650181003.
75. G. Hintzenweg, "Development of the Port of Ziguinchor Survey Report Document short title Survey Report Status Draft report Development of the Port of Ziguinchor," 2013. [Online]. Available: www.royalhaskoningdhv.com
76. "Delft3D 3D/2D modelling suite for integral water solutions User Manual QUICKIN."
77. G. D. Egbert and S. Y. Erofeeva, "Efficient Inverse Modeling of Barotropic Ocean Tides," 2002.
78. G. R. Lesser, *An Approach to Medium-term Coastal Morphological Modelling*. 2009. [Online]. Available: http://www.narcis.nl/publication/RecordID/oai:tudelft.nl:uuid:62caa573-4fc0-428e-8768-0aa47ab612a9
79. JPL D-109532, "SWOT Science Data Products User Handbook," 2024, [Online]. Available: https://epdm.jpl.nasa.gov
80. "SWOT Project SWOT Calibration / Validation Plan Initial Release," 2018. [Online]. Available: https://pdms.jpl.nasa.gov/
81. L. Yu, H. Zhang, W. Gong, and X. Ma, "Validation of Mainland Water Level Elevation Products From SWOT Satellite," *IEEE J Sel Top Appl Earth Obs Remote Sens*, vol. 17, pp. 13494–13505, 2024, doi: 10.1109/JSTARS.2024.3435363.
82. F. Rodrigues Do Amaral, N. Gratiot, T. Pellarin, and T. A. Tu, "Assessing typhoon-induced compound flood drivers: a case study in Ho Chi Minh City, Vietnam," *Natural Hazards and Earth System Sciences*, vol. 23, no. 11, pp. 3379–3405, Nov. 2023, doi: 10.5194/nhess-23-3379-2023.
83. F. R. Do Amaral, T. N. Trung, T. Pellarin, and N. Gratiot, "Challenging SWOT: early assessment of level 2 high-rate river products in an urbanized, low elevation coastal zone," *IEEE Geoscience and Remote Sensing Letters*, 2024, doi: 10.1109/LGRS.2024.3501407.
84. "Surface Water and Ocean Topography (SWOT) Project Release Note Version C KaRIn Science Data Products," 2024. [Online]. Available: https://swotst.aviso.altimetry.fr/fileadmin/user_upload/SWOTST2023/20230922_1_going_forwa

 doi:10.20944/preprints202507.2525.v1

disclaim responsibility for any injury to people or property resulting from any ideas, methods, instructions or products referred to in the content.